FGFR3 overactivation in the brain is responsible for memory impairments in Crouzon syndrome mouse model

Maxence Cornille, Stéphanie Moriceau, Roman H Khonsari, Yann Heuzé, Léa Loisay, Valérie Boitez, Anne Morice, Eric Arnaud, Corinne Collet, Morad Bensidhoum, et al.

JEM Journal of Experimental Medicine

BRIEF DEFINITIVE REPORT

FGFR3 overactivation in the brain is responsible for memory impairments in Crouzon syndrome mouse model

Maxence Cornille[1*], Stéphanie Moriceau[2*], Roman H. Khonsari[1,3], Yann Heuzé[4], Léa Loisay[1], Valérie Boitez[2], Anne Morice[1,3], Eric Arnaud[5], Corinne Collet[6], Morad Bensidhoum[7], Nabil Kaci[1], Nathalie Boddaert[8,9], Giovanna Paternoster[5], Theresa Rauschendorfer[10], Sabine Werner[10], Suzanne L. Mansour[11], Federico Di Rocco[12], Franck Oury[2], and Laurence Legeai-Mallet[1]

Crouzon syndrome with acanthosis nigricans (CAN, a rare type of craniosynostosis characterized by premature suture fusion and neurological impairments) has been linked to a gain-of-function mutation (p.Ala391Glu) in fibroblast growth factor receptor 3 (FGFR3). To characterize the CAN mutation's impact on the skull and on brain functions, we developed the first mouse model (*Fgfr3*$^{A385E/+}$) of this syndrome. Surprisingly, *Fgfr3*$^{A385E/+}$ mice did not exhibit craniosynostosis but did show severe memory impairments, a structurally abnormal hippocampus, low activity-dependent synaptic plasticity, and overactivation of MAPK/ERK and Akt signaling pathways in the hippocampus. Systemic or brain-specific pharmacological inhibition of FGFR3 overactivation by BGJ398 injections rescued the memory impairments observed in *Fgfr3*$^{A385E/+}$ mice. The present study is the first to have demonstrated cognitive impairments associated with brain FGFR3 overactivation, independently of skull abnormalities. Our results provide a better understanding of FGFR3's functional role and the impact of its gain-of-function mutation on brain functions. The modulation of FGFR3 signaling might be of value for treating the neurological disorders associated with craniosynostosis.

Introduction

The members of the fibroblast growth factor receptor (FGFR) family have important roles in bone development and skeletal diseases. Missense mutations in the *FGFR1*, *FGFR2*, and *FGFR3* genes are responsible for a spectrum of craniosynostosis syndromes, characterized by premature fusion of the cranial sutures (Twigg and Wilkie, 2015; Robin et al., 1993). Two dominant *FGFR3* mutations specifically cause Muenke syndrome (MS [MIM 602849], the most common syndromic craniosynostosis; Wilkie et al., 2010) and Crouzon syndrome with acanthosis nigricans (CAN, also referred to as Crouzonodermoskeletal syndrome; MIM 612247).

CAN is a very rare craniosynostosis syndrome (incidence: 1 per 1,000,000) associated specifically with the p.Ala391Glu gain-of-function mutation in *FGFR3* (Meyers et al., 1995), which is known to cause ligand-independent overactivation of *FGFR3* (Li et al., 2006; Chen et al., 2013, 2011). The clinical presentation of CAN resembles that of Crouzon syndrome caused by *FGFR2* mutations (MIM 123500) and includes premature fusion of the coronal sutures, brachycephaly, midfacial hypoplasia, and craniovertebral junction defects. Patients with CAN may also present with acanthosis nigricans, i.e., regionalized hyperpigmentation and thickening of the skin.

[1]Université de Paris, Imagine Institute, Laboratory of Molecular and Physiopathological Bases of Osteochondrodysplasia, Institut National de la Santé et de la Recherche Médicale UMR1163, Paris, France; [2]Institut National de la Santé et de la Recherche Médicale U1151, Institut Necker Enfants-Malades, Depart: Cell growth and Signaling, Université Paris-Sorbonne-Paris Cité, Paris, France; [3]Service de Chirurgie Maxillo-Faciale et Chirurgie Plastique, Hôpital Necker-Enfants Malades, Assistance Publique-Hôpitaux de Paris, Centre de Référence Maladies Rares Fentes et Malformations Faciales MAFACE, Filière Maladies Rares TeteCou, Université de Paris, Paris, France; [4]UMR5199 PACEA, Centre National de la Recherche Scientifique, Ministère de la Culture, Université de Bordeaux, Pessac, France; [5]Service de Neurochirurgie, Hôpital Necker-Enfants Malades, Assistance Publique-Hôpitaux de Paris, Centre de Référence Maladies Rares Craniosténoses et Malformations Craniofaciales CRANIOST, Filière Maladies Rares TeteCou, Université de Paris, Paris, France; [6]Service de Biochimie et Biologie Moléculaire-PôleB2P, Centre Hospitalier Universitaire Paris-GH St-Louis Lariboisière F.Widal-Hôpital Lariboisière, Paris, France; [7]LaboratoireB2OA, Unité Mixte de Recherche CNRS7052, Université de Paris, Paris, France; [8]UMR-1163 Institut Imagine, Hôpital Necker-Enfants Malades, Assistance Publique-Hôpitaux de Paris, Paris, France; [9]Département de Radiologie Pédiatrique, Hôpital Necker-Enfants Malades, Assistance Publique-Hôpitaux de Paris, Paris, France; [10]Institute of Molecular Health Sciences, Eidgenössische Technische Hochschule Zurich, Zurich, Switzerland; [11]Department of Human Genetics, University of Utah, Salt Lake City, UT; [12]Hôpital Femme Mère Enfant Hospices Civils de Lyon, Université Claude Bernard Lyon 1, Lyon, France.

*M. Cornille and S. Moriceau contributed equally to this paper. Correspondence to Laurence Legeai-Mallet: laurence.legeai-mallet@inserm.fr; Correspondence to Franck Oury: franck.oury@inserm.fr.

The FGFR3 is known to be an important regulator of endochondral and membranous ossification. It acts as a negative regulator of long bone growth and regulates the formation and maintenance of skull sutures. During fetal and postnatal development, the skull vault and the brain develop and grow in a coordinated manner (Richtsmeier and Flaherty, 2013). Premature skull vault suture fusion, skull base synchondrosis, and abnormal facial bone growth have several potential consequences, including elevated intracranial pressure in early childhood (Di Rocco et al., 2011; de Planque et al., 2021), hearing and visual impairments, impaired blood flow in the brain, brain malformation, syringomyelia, sleep apnea, and multifactorial developmental delay. Several studies have also reported severe neurological disorders in *FGFR3*-related craniosynostoses, characterized by anxiety and impairments in learning, memory, attention, and emotional control (Maliepaard et al., 2014; Yarnell et al., 2015; Kruszka et al., 1993). Interestingly, *Fgfr3* is expressed strongly in the central nervous system and notably in the hippocampus—a brain structure that is essential for the control of cognitive functions like learning and memory (Peters et al., 1993; Bansal et al., 2003; Itoh et al., 2013). FGFR3 is thought to promote neurogenesis and to regulate the onset of astroglial and oligodendrocyte differentiation (Pringle et al., 2003; Oh et al., 2003; Levenga et al., 2017; Vithayathil et al., 2015; Dabrowski et al., 2015); however, its functional relevance in the brain has not yet been characterized.

Here, we generated the first mouse model of CAN and then sought to determine the FGFR3's role in the syndrome's pathogenesis in the skull and the brain. The $Fgfr3^{A385E/+}$ mouse ubiquitously expresses a dominant p.Ala385Glu mutation in *Fgfr3*. We analyzed the model's skeletal and neurological phenotypes and administered a series of behavioral tests. We found that mutant mice did not reproduce the skull phenotype seen in CAN but did exhibit severe learning and memory impairments, which were associated with low synaptic plasticity and overactivation of the FGFR3's downstream pathways (Erk1/2 and AKT) in the hippocampus. Importantly, we showed that the brain-selective administration of a high-affinity FGFR tyrosine kinase inhibitor (BGJ398) in $Fgfr3^{A385E/+}$ rescued the animals' cognitive impairments. Taken as a whole, our study results (i) demonstrate that a *FGFR3* gain-of-function mutation leads to learning and memory impairments independently of skull abnormalities and (ii) suggest that modulation of the FGFR3 signaling pathway might be of value for treating the neurological and cognitive impairments observed in craniosynostosis.

Results and discussion

The $Fgfr3^{A385E/+}$ CAN model's skull phenotype is essentially normal

We generated the first mouse model ($Fgfr3^{A385E/+}$) of CAN. The mice were designed to express a p.Ala385Glu missense mutation located in the Fgfr3's transmembrane domain (corresponding to the p.Ala391Glu mutation in humans). We then assessed the CAN mutation's impact on the development of the skull (Fig. 1 A). The *Fgfr3* p.Ala385Glu transcripts were detected in calvarial osteoblasts (Fig. 1 B). Micro CT (µCT) experiments showed (surprisingly) that the $Fgfr3^{A385E/+}$ mice had normal craniofacial features (Fig. 1 C). The coronal sutures and skull base synchondroses were patent at postnatal day (P) 21, just as they were in control mice (Fig. 1 C). We also investigated the skull phenotype in CAN patients. We observed brachycephaly (as a result of premature coronal suture fusion), oculo-orbital disproportion, premature fusion of the anterior-intra-occipital synchondroses (Fig. 1 D), prognathism, and midfacial hypoplasia (Fig. S1, A–C). These phenotypic traits are similar to those seen in Crouzon syndrome (MIM 123500) caused by *FGFR2* mutations (Coll et al., 2018, 2016; Di Rocco et al., 2011).

In order to understand the absence of premature closure of the coronal suture in CAN mice, we assessed the functional status of calvarial $Fgfr3^{A385E/+}$ osteoblasts in vitro. There were no significant differences in mineralization capacity, proliferation, and mitogen-activated protein kinase (MAPK) activation between osteoblasts from $Fgfr3^{A385E/+}$ mice and control osteoblasts (Fig. S2, A–D). We next analyzed the mandibular phenotype in $Fgfr3^{A385E/+}$ and $Fgfr3^{+/+}$ mice, using landmark-based geometric morphometry (Heuzé et al., 2010). Although there were no significant differences in skull shape (Procrustes distance [d] = 0.0148; P = 0.0940), there was a significant intergroup difference in the shape of the mandible (d = 0.0159; P < 0.01; Fig. 1 E) on P21 (but not on P90 or P180; skull: P21 d = 0.0148, NS, P90 d = 0.0136, NS, P180 d = 0.0136, NS; mandible: P21 d = 0.0159, P < 0.01, P90 d = 0.0191, NS, P180 d = 0.0176, NS). In CAN patients, we also observed a growth defect of the mandible in general and the mandibular symphysis in particular (Figs. 1 F and S1 C). The relatively small mandible and the severe maxillary retrusion confirmed that people with CAN have class III malocclusion (Morice et al., 2020). These observations corroborate the mandibular changes observed in our CAN mouse model and reinforce the hypothesis whereby FGFR3 gain-of-function mutations have an intrinsic effect on the mandible's morphology.

No obvious defects in the appendicular and axial skeleton were observed in fetal or newborn $Fgfr3^{A385E/+}$ mice (data not shown) or in adult $Fgfr3^{A385E/+}$ mice; this result is in line with the human disease (Fig. 1 G). We confirmed these data on µCT images of femurs from 3-mo-old $Fgfr3^{A385E/+}$ mice; the structure of the trabecular and cortical bones was normal (Fig. S2 E).

In people with CAN, the skull abnormalities caused by premature fusion exert mechanical pressure on the brain and tend to increase the intracranial pressure (Al-Namnam et al., 2019). The premature fusion of skull vault sutures is associated with structural abnormalities in the brain, including gyration defects in the cortical area and the corpus callosum in CAN, and abnormal hippocampal structure in MS (Grosso et al., 2003; Gürbüz et al., 2016; Okubo et al., 2017). These impairments in brain growth have been also linked to functional problems, such as visual, hearing, and cognitive impairments (Di Rocco et al., 2011; Martínez-Abadías et al., 2011). Here, we observed compression of the brain and disorganization of the parahippocampal groove in patients with CAN (Fig. 1 H). These defects have not previously been described in the literature and might correspond to a significant phenotypic trait in CAN. Magnetic resonance imaging of the $Fgfr3^{A385E/+}$ mouse's brain at 4 mo of age did not evidence any differences in hippocampal

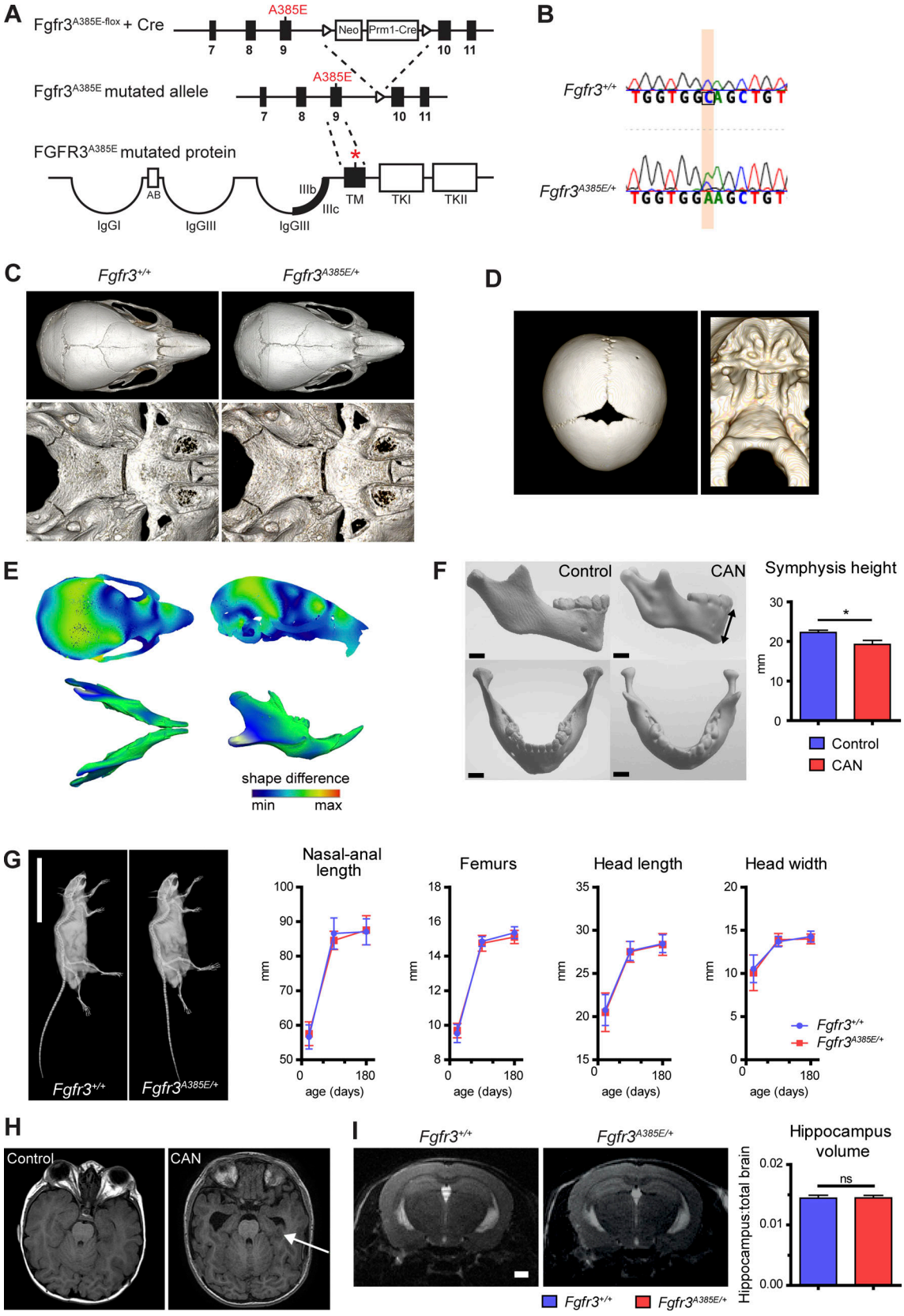

Figure 1. **Normal skeletal development of *Fgfr3*$^{A385E/+}$ mice, compared with human CAN. (A)** Using a cassette with the neomycin gene (NEO) flanked by LoxP sites, the p.Ala385Glu point mutation was inserted into exon 9 of *Fgfr3* through homologous recombination in embryonic stem cells. Once the germline insertion had been established, the Prm1 promoter enabled the cassette to be excised in the male germline at the first generation. **(B)** Presence of the heterozygous mutation p.Ala385Glu in RNA isolated from calvarial osteoblasts. **(C)** µCT of mice at P21, showing a normal skull morphology for the *Fgfr3*$^{+/+}$

mouse. Cranial sutures and skull base synchondroses were patent for the *Fgfr3*$^{A385E/+}$ mouse. **(D)** CT scan of patient #2 at 1 yr of age, showing a partial lambdoid fusion. The skull base presents prematurely fused anterior-intraoccipital synchondroses. **(E)** 3D rendering (heat map) of differences in shape between *Fgfr3*$^{+/+}$ and *Fgfr3*$^{A385E/+}$ mice for the skull and the mandible (studied separately) at P21. Morphometric analysis was performed on µCT data acquired from *Fgfr3*$^{A385E/+}$ mice and control littermates on P21, P90, and P180. There were no significant differences in skull shape between *Fgfr3*$^{A385E/+}$ and control animals at any of the three time points. The only significant difference in mandible shape between *Fgfr3*$^{A385E/+}$ and control animals was noted on P21 (d = 0.0159; P < 0.01; P21: *Fgfr3*$^{+/+}$, n = 9; *Fgfr3*$^{A385E/+}$, n = 8; P90: *Fgfr3*$^{+/+}$, n = 10; *Fgfr3*$^{A385E/+}$, n = 8; P180: *Fgfr3*$^{+/+}$, n = 9; F *Fgfr3*$^{A385E/+}$, n = 8). **(F)** 3D reconstructed CT images of the mandible in a female patient with CAN at the age of 2 yr and 3 mo, and in an age- and sex-matched control (scale bar: 10 mm). Measurements of mandibular features (quoted as the median [IQR]) revealed that the mandibular symphysis was unusually short (P = 0.02) in four patients with CAN (median [IQR] age: 22.7 mo [12.6; range: 8–31.3]), relative to four age- and sex-matched controls. **(G)** X-rays of 3-mo-old animals, showing a normal skeletal phenotype in *Fgfr3*$^{A385E/+}$ mice (n = 8) relative to the WT *Fgfr3*$^{+/+}$ (n = 9). Scale bar: 5 cm. Nasal–anal distance, femur length, skull length, and skull width measurements in males measured on P21, 90, and 180 (P21: *Fgfr3*$^{+/+}$, n = 11; *Fgfr3*$^{A385E/+}$, n = 10; P90: *Fgfr3*$^{+/+}$, n = 10; *Fgfr3*$^{A385E/+}$, n = 12; P180: *Fgfr3*$^{+/+}$, n = 10; F *Fgfr3*$^{A385E/+}$, n = 12). **(H)** Transverse plane brain MRI of a 2-yr-old control subject (left) and CAN patient #1 (right) at the age of two, showing compression of the brain and disorganization of the parahippocampal groove (arrow; n = 3 out of 3). **(I)** Representative brain MRI of 4-mo-old animals. No morphological abnormalities were observed for mutant mice (*Fgfr3*$^{+/+}$, n = 5; *Fgfr3*$^{A385E/+}$, n = 7). Scale bar: 1 mm. Data are expressed as the mean ± SEM. *, P ≤ 0.05. A two-tailed Student's t test was used to compare patient groups and the control group. An unpaired Student's t test was used to compare groups of animals.

volume or any compression of brain structures—suggesting that the brain develops normally in our mouse model of CAN (Fig. 1 I).

With regard to the patients' skin, acanthosis nigricans is observed in skin folds in the neck and axillary regions (Fig. S1, A and D). Histologic assessments of skin biopsies from CAN patients (relative to a control sample) revealed severe hyperkeratosis, severe hyperplasia, and cyst formation at the hair follicles. Having observed the expression of FGFR3 in CAN skin, we also analyzed the MAPK pathway downstream of FGFR3. The Erk1/2 phosphorylation level was higher in acanthotic areas than in unaffected areas—thus confirming the high activity of the FGFR3 variant in the skin (Fig. S1 D). No signs of hyperkeratosis or changes in epidermal thickness or pigmentation were detected in *Fgfr3*$^{A385E/+}$ mice, and there were no obvious differences in FGFR3 expression or Erk1/2 activation in the skin (Fig. S2 F). We also examined the cochlea because the gain of FGFR3 activity in mouse models of achondroplasia and in MS changes the fate of cochlear cells and causes hearing loss (Pannier et al., 2009; Mansour et al., 2013). The distributions of sensory cells (labeled with MYO7A) and supporting cells (labeled with PROX1, CD44, and p75NTR) in the *Fgfr3*$^{A385E/+}$ organ of Corti were normal (Fig. S2 G).

In the present study, we found that the *Fgfr3*$^{A385E/+}$ mouse model of CAN lacked the major cranial malformations typically associated with the human disorder. Interestingly, the *Fgfr3*$^{A385E/+}$ mouse's skull phenotype was similar to that described for a mouse model of MS (*Fgfr3*$^{P244R/+}$). Indeed, the sutures and synchondroses were found to be slightly affected in the *Fgfr3*$^{P244R/+}$ mice, and the coronal suture was fused in a small proportion of individuals (Twigg et al., 2009; Laurita et al., 2011). Interestingly, *Fgfr3* knock-out (*Fgfr3*$^{-/-}$) was not associated with an abnormal craniofacial phenotype (Colvin et al., 1996; Deng et al., 1996; Su et al., 2010) whereas the zebrafish *Fgfr3*$^{lof/lof}$ exhibited major changes in the skull (a lack of sutures, abnormal frontal and parietal bones, and the presence of ectopic bones; Dambroise et al., 2020; Cornille et al., 2019). Taken as a whole, these observations in *Fgfr3* animal models emphasize the differences in the receptor's roles in craniofacial development in humans, mice, and zebrafish; for example, it appears that FGFR3 is less involved in intramembranous ossification in mice than in humans but is strongly involved in zebrafish. Furthermore, these observations emphasize *Fgfr3*'s pleiotropic role and the receptor's interaction with other proteins. As has been reported for other cases of craniosynostosis, the phenotype appears to depend on the Fgfr3 mutation (Timberlake et al., 2016, 2019).

The *Fgfr3*$^{A385E/+}$ mouse displays impairments in learning and memory

In humans, the premature fusion of skull vault sutures is associated with structural abnormalities in the brain (Grosso et al., 2003; Gürbüz et al., 2016; Okubo et al., 2017). A study of a large group of MS patients reported impairments in adaptive and executive functions, including working memory impairments, attention deficit hyperactivity disorder, and (in all patients) impaired emotional control (Yarnell et al., 2015). In animal studies, the *Fgfr3*$^{+/K644E}$ mouse model of thanatophoric dysplasia (with the mutant protein expressed either ubiquitously or under the control of the Nestin promoter) shows severe overgrowth of the cerebellum and cortex, whereas *Fgfr3*$^{-/-}$ mice presented an underdeveloped neocortex (Inglis-Broadgate et al., 2005; Moldrich et al., 2011; Thomson et al., 2009, 2007). These observations are in line with the known role of fibroblast growth factor and the FGFR in the development of the hippocampus (Iwata and Hevner, 2009; Ohkubo et al., 2004; Stevens et al., 2012; Zhao et al., 2007). However, it is widely accepted that the abnormal brain morphology and cognitive impairments observed in craniosynostoses are related to the premature fusion of cranial sutures and the chronic increase in intracranial pressure (Aldridge et al., 2010; Arnaud-López et al., 2007; Gürbüz et al., 2016; Martínez-Abadías et al., 2011). It is noteworthy that a recent study of the Twist$^{+/-}$ mouse model of Saethre-Chotzen craniosynostosis syndrome also found that suture fusion resulted in elevated intracranial pressure, together with social and memory impairments. The Twist$^{+/-}$ mouse's craniofacial and behavioral phenotype was rescued by suture stem cell engraftment (Yu et al., 2021).

Here, by taking advantage of the absence of an abnormal skull phenotype in the *Fgfr3*$^{A385E/+}$ mouse (Fig. 1 C), we were able to directly analyze the role of an activating *Fgfr3* gain-of-function mutation in the brain. Importantly, the *Fgfr3*$^{A385E/+}$ mouse's brain did not present severe morphological modifications, which suggested that the *Fgfr3*^{A385E} mutation does not significantly impact brain development and cognition. To explore *Fgfr3*'s role in the hippocampus, we subjected *Fgfr3*$^{A385E/+}$ mice and their

control littermates to a series of behavioral tests. Before executing the tests, we confirmed the heterozygous *Fgfr3*^{A385E} mutation was indeed expressed in the mutant mouse's hippocampus (Fig. S3 A). Hence, we then evaluated cognitive functions that require an intact hippocampus (Glatigny et al., 2019): episodic memory (using the novel object recognition [NOR] test), associative memory (using one-trial contextual fear conditioning, CFC), spatial memory (using the Morris water maze [MWM] and novel object location [NOL] tests), and exploratory and anxiety-like behaviors (using the open field test [OFT] and the light/dark test [L/DT]; Fig. 2, A–D).

It has been shown that in a modified version of the NOR test (Denny et al., 2012; Ennaceur and Delacour, 1988), control mice are capable of differentiating between novel objects and familiar objects and tend to explore novel objects for longer. Remarkably, and as shown in Figs. 2 A and S3 C, we found that 4-mo-old *Fgfr3*$^{A385E/+}$ mice explored novel objects significantly less than controls did. In the CFC test, the *Fgfr3* gain-of-function mutation was associated with a shorter context-elicited freezing time during the testing phase (relative to control littermates)—indicating that contextual fear memory is impaired in the mutant *Fgfr3*$^{A385E/+}$ mouse (Fig. 2 B). However, the mutant mice displayed normal results for spatial learning, memory (in the NOL test and the MWM; Fig. S3, B, D, and E), and anxiety- and exploratory-like behaviors (in the OFT and the L/DT; Fig. 2, C and D).

In humans and mice, learning impairments and altered mood are often associated with a low hippocampal volume (Kitamura and Inokuchi, 2014). To further explore the hippocampal structures, we performed neuronal nuclei protein (NeuN) immunofluorescence on hippocampus sections. The volume of the granular layer of the hippocampal dentate gyrus (DG) was significantly lower in 4-mo-old *Fgfr3*$^{A385E/+}$ mice than in control mice, whereas there were no volume differences in the cornu ammonis (CA)1 and CA3 regions (Fig. 2 E). The abnormally low volume in the DG—a key structure for learning and memory processes—is in line with the behavioral defects observed in *Fgfr3*$^{A385E/+}$ mice. The FGFR3 protein levels were slightly elevated in the *Fgfr3*$^{A385E/+}$ hippocampus (Fig. 2, F and G), and we did not observe defects in apoptosis (using ApopTag immunolabeling) or adult neurogenesis (using doublecortin immunolabeling) in the *Fgfr3*$^{A385E/+}$ hippocampus, relative to controls (Fig. S3 G).

Taken together, our results demonstrate that *Fgfr3*$^{A385E/+}$ mice exhibited severe impairments in working and episodic memory but were free of locomotor problems and anxiety-related behavioral disorders. According to the literature, other FGFR family members are also involved in hippocampus-dependent learning and memory. Deletion of *Fgfr2* in embryonic and adult mice specifically affected long- and short-term spatial memory, as a result of poor neurogenesis in the hippocampus (Stevens et al., 2012). Similarly, deletion of *Fgfr1* impaired working and contextual memory (when driven by hGFAP-Cre) and spatial memory (when driven by Nestin-cre) and, in one case, was associated with a low DG volume (Müller Smith et al., 2008; Ohkubo et al., 2004; Zhao et al., 2007). The present study is the first demonstration that expression of an *Fgfr3* gain-of-function mutation in the murine hippocampus is associated with learning and memory impairments.

Lower activity-dependent synaptic plasticity in hippocampal neurons and modification of the signaling pathways in *Fgfr3*$^{A385E/+}$ mice

Previous research had demonstrated that the PI3K-Akt and MAPK signaling pathways are regulated in the growth plate cartilage following FGFR3 activation (Komla-Ebri et al., 2016; Priore et al., 2006). We hypothesized that the memory impairments in the *Fgfr3*$^{A385E/+}$ mouse were due to abnormal *Fgfr3* activity in the hippocampus (Fig. 3 A). Accordingly, we first observed abnormally high levels of phosphorylated Erk1/2 and Akt proteins (Fig. 3, B and C); this confirmed that the *Fgfr3*^{A385E} mutation indeed activated pathways downstream of FGFR3 in the hippocampus.

It is well known that associative memory ability is related to activity-dependent synaptic plasticity in hippocampal neurons. We assessed dendritic spine density in WT and *Fgfr3*$^{A385E/+}$ mice having been exposed to CFC for 4 d consecutively; in WT mice, this protocol is known to enhance dendritic spine formation in the granular layer neurons of the hippocampal DG. As a result, Golgi staining showed that dendritic spine formation was significantly induced in control but not in *Fgfr3*$^{A385E/+}$ hippocampal DG (Fig. 3 D). Lastly, we assessed the expression of key markers of synaptic plasticity (c-Fos, CAMK2, and CREB) in the hippocampus (Minatohara et al., 2015; Sakamoto et al., 2011; Shioda and Fukunaga, 2017). We found that levels of c-Fos, phosphorylated and native CAMK2 (CAMK2-P and CAMK2), and phosphorylated CREB proteins were significantly lower in *Fgfr3*$^{A385E/+}$ mice than in control mice (Fig. 3 E).

Taken together, our data demonstrate that the *Fgfr3*^{A385E} mutation influenced episodic memory and associative fear memory, and induced alteration of pre-synaptic plasticity in hippocampal neurons. This observation reinforces the notion whereby hippocampal fibroblast growth factor signaling pathways have a key role in the maintenance of neuronal plasticity and integrity, as suggested previously (Dabrowski et al., 2015; Levenga et al., 2017; Vithayathil et al., 2015).

Selective inhibition of Fgfr3 in the brain rescues the memory impairments observed in *Fgfr3*$^{A385E/+}$ mice

To confirm the direct involvement of brain *Fgfr3* in the memory disorders observed in *Fgfr3*$^{A385E/+}$ mice, we decided to inhibit the receptor. Previous research had shown that subcutaneous injections of a high-affinity, *Fgfr3*-specific tyrosine kinase inhibitor (BGJ398) inhibited *Fgfr3* overactivation and rescued the phenotype of an *Fgfr3*-related mouse model of achondroplasia bearing a *Fgfr3*$^{Y367C/+}$ gain-of-function mutation (Komla-Ebri et al., 2016). We hypothesized that BGJ398 could have a similar effect on mice with a CAN-causing mutation. To confirm this hypothesis, we transiently transfected HEK293 cells with human *FGFR3*^{A391E} cDNA. As a result, we observed a significantly greater phosphorylation level of the receptor and the downstream Erk1/2 signaling pathway than in controls (Fig. 4, A and B). In line with data obtained previously with other FGFR3 variants, we observed that treatment with BGJ398 restored FGFR3^{A391E} activity to control levels and thus decreased the phosphorylation of Erk1/2 (Fig. 4, A and B).

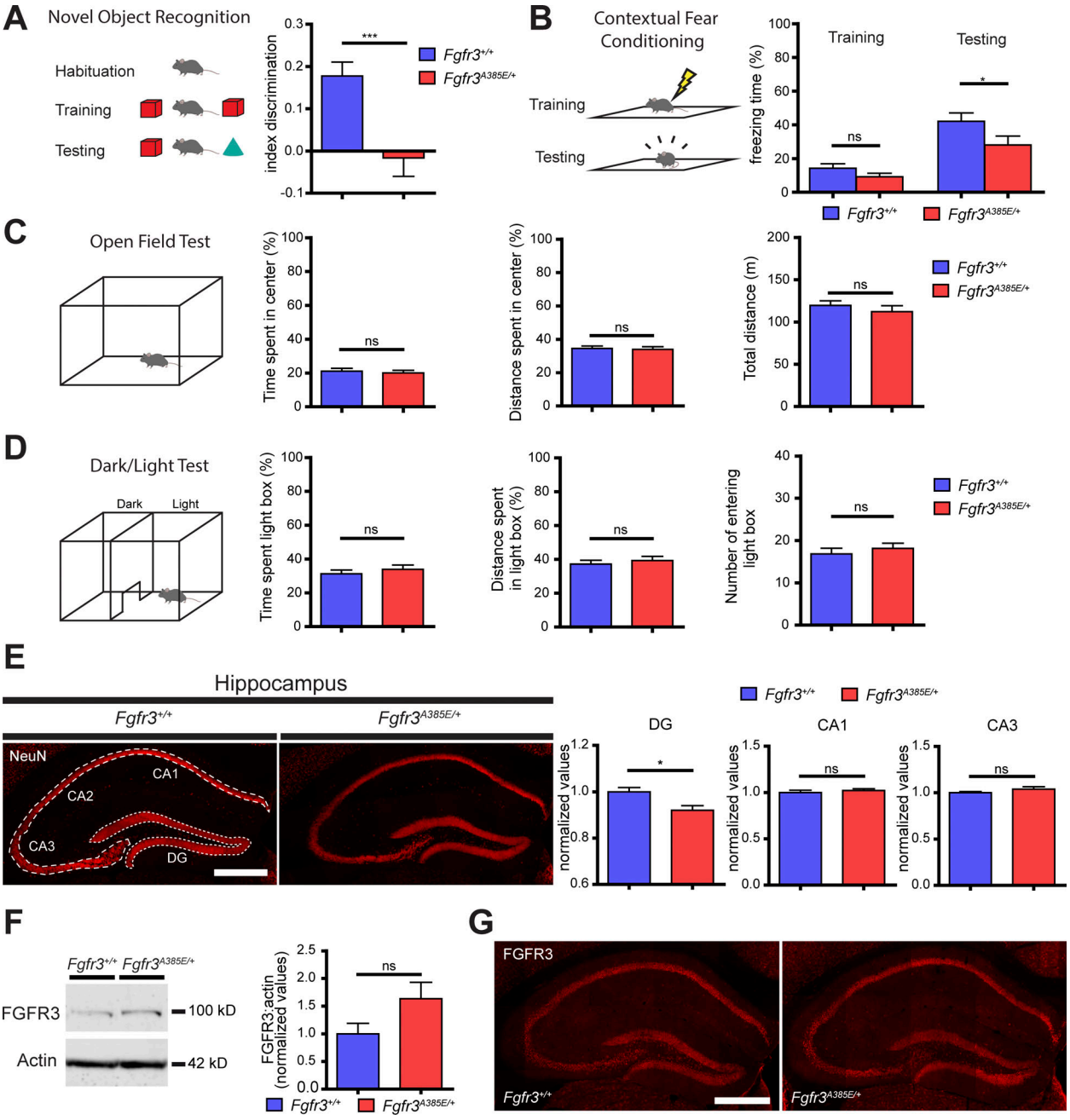

Figure 2. **The *Fgfr3*$^{A385E/+}$mouse model shows hippocampus-associated memory impairments. (A)** The NOR test in 4-mo-old male mice. The discrimination index was measured 24 h after the training phase, in order to assess the memory performance of two independent groups of *Fgfr3*$^{A385E/+}$ mice (n = 17) and their control littermates (n = 14). **(B)** CFC performed in two independent groups of 4-mo-old male mice (*Fgfr3*$^{+/+}$, n = 13; *Fgfr3*$^{A385E/+}$, n = 12). The proportion of time freezing was recorded during the training phase (as a control for the baseline level) and the test phase (to assess memory performance). **(C)** The OFT performed in *Fgfr3*$^{+/+}$ (n = 17) and *Fgfr3*$^{A385E/+}$ (n = 14) mice. Total distance traveled (meters), the proportion of distance traveled in the center versus the periphery, and the proportion of time spent in the center versus the periphery were measured. **(D)** The L/DT performed in *Fgfr3*$^{+/+}$ (n = 17) and *Fgfr3*$^{A385E/+}$ (n = 14) mice. The number of entries into the lit compartment, the proportion of distance traveled in the lit compartment, and the proportion of time spent in the lit compartment were measured. **(E)** Immunofluorescence labeling of NeuN in the brain of 4-mo-old mice. Volume of NeuN labeling in the DG region was significantly lower in *Fgfr3*$^{A385E/+}$mice (n = 6) than in *Fgfr3*$^{+/+}$mice (n = 7); volume was determined by area measurements of the different regions on successive brain sections. Data were normalized against *Fgfr3*$^{+/+}$. Scale bar: 100 µm. **(F)** Expression of FGFR3 in hippocampus lysates from 4-mo-old mice (*Fgfr3*$^{+/+}$, n = 5; *Fgfr3*$^{A385E/+}$, n = 5). **(G)** Immunofluorescence labeling of FGFR3 in the brain of 4-mo-old mice. The FGFR3 expression patterns were similar for *Fgfr3*$^{A385E/+}$ (n = 5) and *Fgfr3*$^{+/+}$ (n = 5) mice. Scale bar: 100 µm. All behavioral tests were performed on two independent cohorts of mice for each group. Data are expressed as the mean ± SEM. *, P < 0.05; ***, P < 0.001. ns, not significant in a two-tailed Student's t test, relative to the control group.

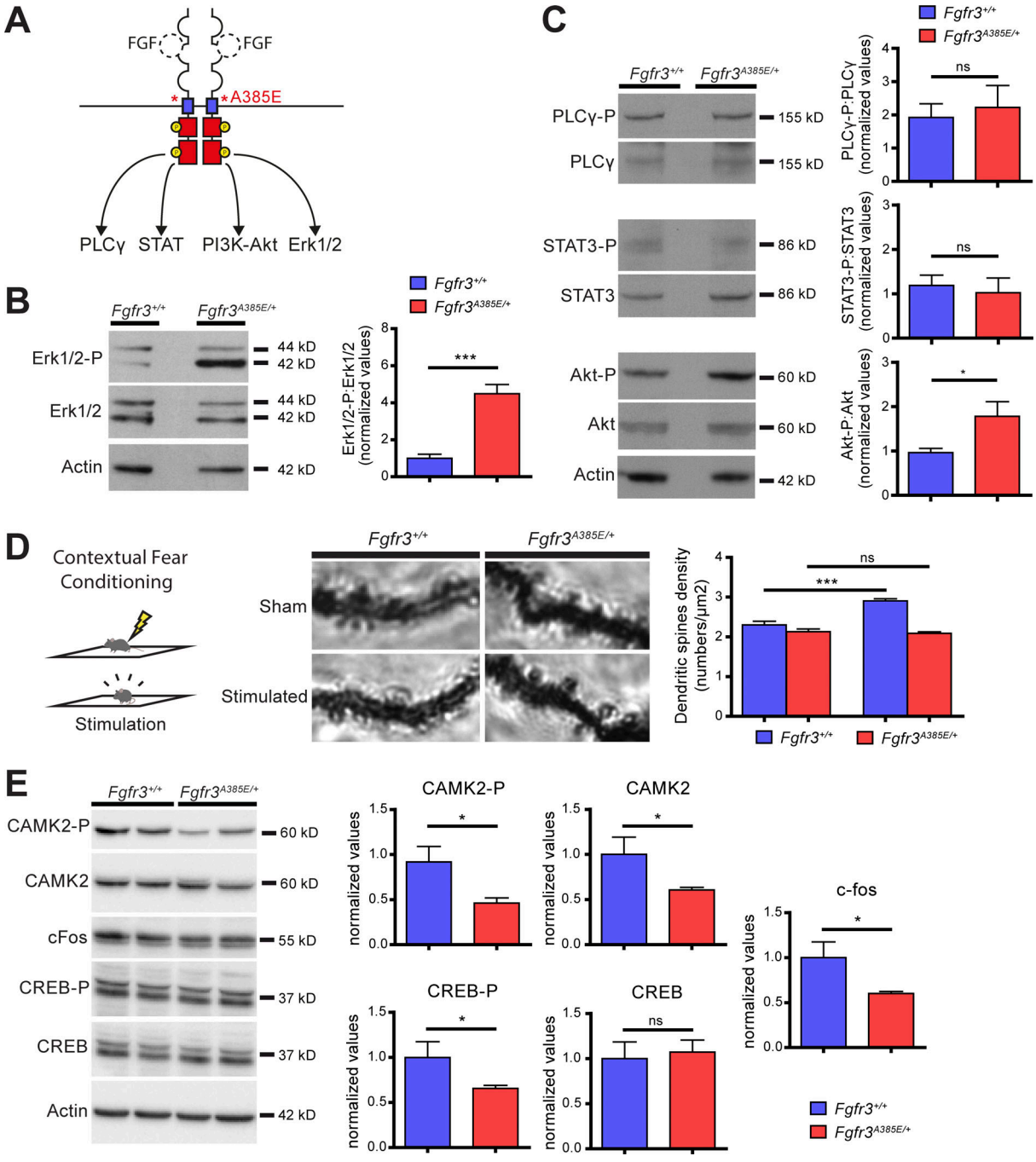

Figure 3. **Overactivation of FGFR3 signaling pathway in the hippocampus is associated to decreased synaptic plasticity in *Fgfr3*$^{A385E/+}$ mice. (A)** A schematic representation of CAN-associated overactivation of FGFR3 and downstream signaling. BGJ398 strongly inhibits FGFR3 phosphorylation. **(B)** Expression of phosphorylated ERK1/2 in the hippocampus. The *Fgfr3*$^{A385E/+}$ mutant showed significantly greater phosphorylation levels (*Fgfr3*$^{+/+}$, $n = 10$; *Fgfr3*$^{A385E/+}$, $n = 9$). **(C)** Expression of total and phosphorylated forms of PLCg, STAT3, and Akt (*Fgfr3*$^{+/+}$, $n = 10$; *Fgfr3*$^{A385E/+}$, $n = 9$). **(D)** Memory-related stimulation and Golgi-Cox staining. The *Fgfr3*$^{A385E/+}$ mutant did not display the induction of dendritic spine formation (*Fgfr3*$^{+/+}$ + sham, $n = 5$; *Fgfr3*$^{+/+}$ + stimulation, $n = 5$; *Fgfr3*$^{A385E/+}$ + sham, $n = 5$; *Fgfr3*$^{A385E/+}$ + stimulation, $n = 5$). **(E)** Expression of key markers of synaptic plasticity in the hippocampus. The *Fgfr3*$^{A385E/+}$ mutant showed significantly lower phosphorylation levels for c-fos, phosphorylated CAMK2, native CAMK2, and phosphorylated CREB, relative to the WT. (*Fgfr3*$^{+/+}$, $n = 5$; *Fgfr3*$^{A385E/+}$, $n = 5$). Data were normalized against the level of actin. All behavioral tests were performed on two independent cohorts of mice for each group. Data are expressed as the mean ± SEM. *, $P \le 0.05$; ***, $P \le 0.001$; ns, not significant in a two-tailed Student's *t* test, relative to the control group.

To confirm that memory impairments in *Fgfr3*$^{A385E/+}$ mice were due to increased activation of FGFR3 in the central nervous system, we next determined whether or not selective inhibition of the receptor in the brain of *Fgfr3*$^{A385E/+}$ mice via BGJ398 reduced the cognitive impairments observed in these mice (Gudernova et al., 2015; Komla-Ebri et al., 2016). To this end,

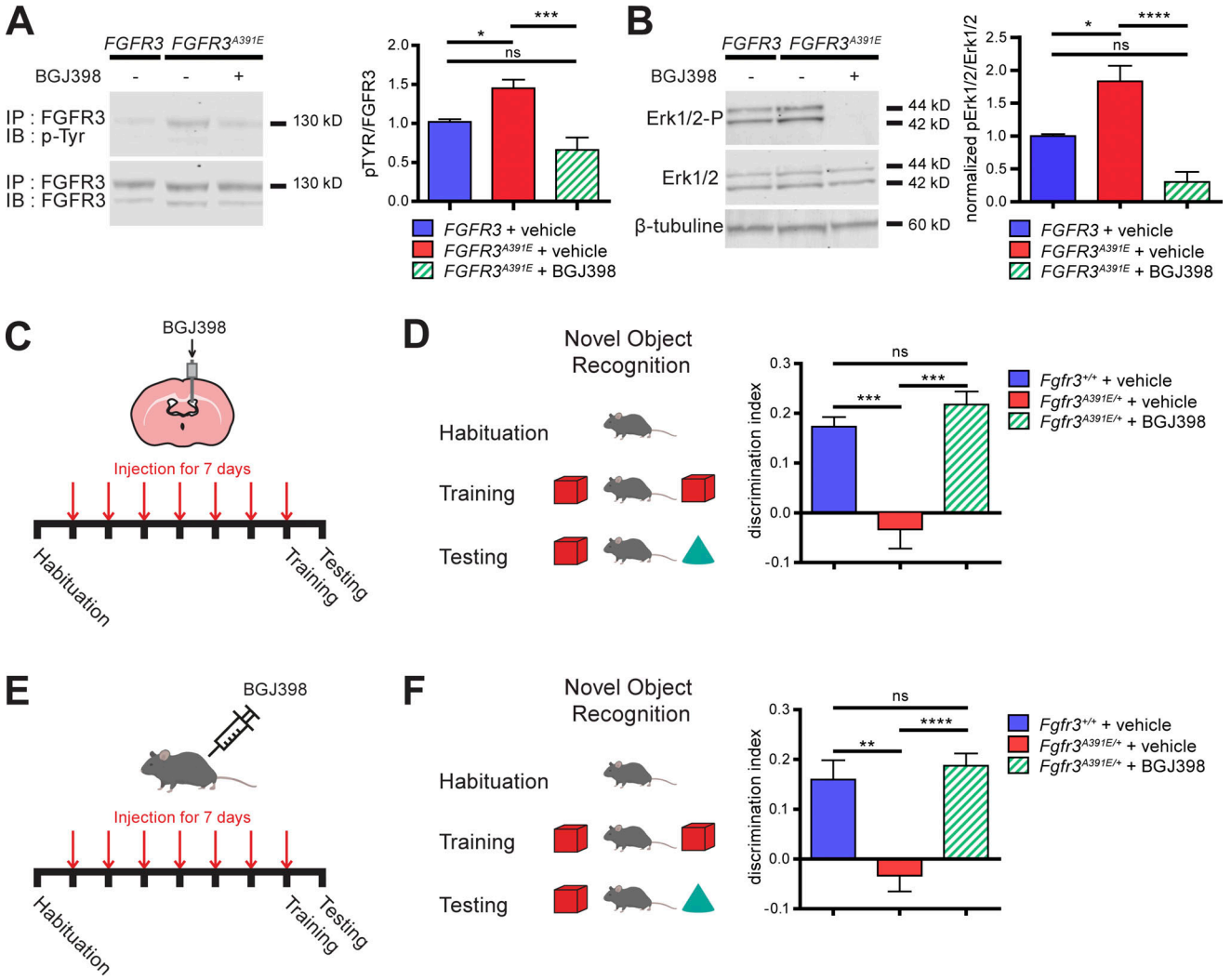

Figure 4. **Downregulation of *Fgfr3*$^{A385E/+}$ phosphorylation rescued the memory impairment. (A)** Phosphorylated FGFR3 and total FGFR3 expression levels in HEK293 cells transfected with FGFR3 or FGFR3^{A391E} and treated with either BGJ398 or vehicle (transfection number: FGFR3 + vehicle, *n* = 7; FGFR3^{A391E} + vehicle, *n* = 7; FGFR3^{A391E} + BGJ398, *n* = 7). **(B)** Expression of phosphorylated ERK1/2 in transfected HEK293 cells (*FGFR3* + vehicle, *n* = 8; *FGFR3*^{A391E} + vehicle, *n* = 9; *FGFR3*^{A391E} + BGJ398, *n* = 6). **(C)** Schematic representation of the experimental procedure for the behavioral tests performed in *Fgfr3*$^{A385E/+}$ mice or control littermates (*Fgfr3*$^{+/+}$) after daily ICV injections (for 7 d) with either BGJ398 or vehicle. The NOR test's training session took place 1 h after the last injection. **(D)** The NOR test in 4-mo-old *Fgfr3*$^{A385E/+}$ or *Fgfr3*$^{+/+}$ mice after 7 d of ICV injections of either BGJ398 or vehicle (*Fgfr3*$^{+/+}$ + vehicle, *n* = 15; *Fgfr3*$^{A385E/+}$ + vehicle, *n* = 14; *Fgfr3*$^{A385E/+}$ + BGJ398, *n* = 14). The discrimination index was measured for each group during the testing phase. The NOR test was performed on two independent cohorts of mice for each group. **(E)** Schematic representation of the experimental procedure for the behavioral tests performed after daily intraperitoneal injection (for 7 d) with either BGJ398 or vehicle. The NOR test's training session took place 1 h after the last injection. **(F)** The NOR test in 4-mo-old *Fgfr3*$^{A385E/+}$ or *Fgfr3*$^{+/+}$ mice after 7 d of intraperitoneal injections of either BGJ398 or vehicle (*Fgfr3*$^{+/+}$ + vehicle, *n* = 15; *Fgfr3*$^{A385E/+}$ + vehicle, *n* = 8; *Fgfr3*$^{A385E/+}$ + BGJ398, *n* = 9). The discrimination index was measured for each group during the testing phase. The NOR test was performed on two independent cohorts of mice for each group. Data are expressed as the mean ± SEM. *, P < 0.05; **, P < 0.01; ***, P < 0.001; ****, P < 0.0001. ns, not significant in a two-way repeated-measures ANOVA, followed by Tukey's post-hoc test for multiple comparisons, for pairwise differences between groups of mice.

4-mo-old *Fgfr3*$^{A385E/+}$ mice and their control littermates received daily intracerebroventricular (ICV) injections of either the specific tyrosine kinase inhibitor BGJ398 (Gudernova et al., 2015; Komla-Ebri et al., 2016) or vehicle solution for 7 d and then underwent the NOR test (Fig. 4 C). We found that postnatal BGJ398 injections were sufficient to rescue the memory impairments observed in *Fgfr3*$^{A385E/+}$ mice (Figs. 4 D and S3 F). We further confirmed these results by giving *Fgfr3*$^{A385E/+}$ mice daily systemic (intraperitoneal) injections of BGJ398 for 7 d (Fig. 4, E and F). Both systemic and ICV administrations of BGJ398 rescued the impairments in associative and working memory observed in adult *Fgfr3*$^{A385E/+}$ mice. These observations confirmed that intraperitoneally administered BGJ398 is able to cross the blood–brain barrier and target FGFR3.

Together, the BGJ398-induced rescue, the absence of craniocerebral disproportion, and thus the probable lack of intracranial hypertension in *Fgfr3*$^{A385E/+}$ mice prompt us to conclude that the memory impairments observed in *Fgfr3*$^{A385E/+}$ mice were directly due to the mutation's impact on the brain.

Our study is the first to have evidenced a direct impact of an *Fgfr3* gain-of-function mutation on memory performance and thus provides a possible explanation for the neurological disorders observed in people with CAN. Moreover, the observed effects of intraperitoneal and ICV administration of the *Fgfr3* inhibitor BGJ398 in adult mice strongly suggest that FGFR3 has a postnatal role in the brain for the control of cognitive functions.

In summary, our results showed that the FGFR3 A385E gain-of-function mutation associated with CAN in humans does not lead to craniosynostosis phenotype in mice but does have a significant impact on learning and memory abilities. Our study is the first to demonstrate that *Fgfr3* has a role in controlling cognition and synaptic plasticity and thus emphasized the physiological importance of the FGF and FGFR families in the brain. These unprecedented results further indicate that the behavioral impairments observed in people with CAN might be due to a craniosynostosis-independent, brain-intrinsic effect of the FGFR3 mutation. This concept is also in line with a hypothesis raised several years ago, in which certain cognitive impairments found in patients with FGFR-related synostosis are caused by abnormal FGFR expression in the brain—rather than through an effect of skull size or the associated hydrocephalus (Raybaud and Di Rocco, 2007). Importantly, we found that inhibition of the FGFR3 signaling pathway in the brain rescues the learning and memory impairments observed in the CAN mouse model. This phenotypic trait and other findings warrant further investigation, with a view to (i) providing better care for people with FGFR3-related craniosynostosis syndromes and (ii) developing novel therapeutic approaches for neurological and cognitive impairments in people with craniosynostosis.

Materials and methods

Patient imaging

Four people diagnosed with CAN (mutation: p.Ala391Glu) were included in the study after they (or their parents) had provided their informed consent. Patient #1 underwent a clinical examination and T2-weighted magnetic resonance imaging (MRI; GE 1.5T Optima MR450W) at 2 yr of age. T2-weighted MRI data from an age-matched control case were also included in our analysis, again after the provision of informed consent by the parents. Coronal sections of the MRI datasets were reconstructed using Carestream PACS software (version 11.0; Carestream Health).

After the provision of informed consent, a computed tomography (CT) scan (acquired on a 64-slice CT system; LightSpeed VCT; General Electric Medical Systems) of patient #2 at the age of 1 yr was imported with Mimics software (version 20.0; Materialise) and segmented for rendering purposes.

Additional CT scans from the four patients with CAN and from four age- and sex-matched controls were used to measure mandibular dimensions. Segmentation and three-dimensional (3D) reconstruction were performed on the raw DICOM data using 3D Slicer (version 4.10.2), after the mandible had been contoured on the basis of its cortical and trabecular bone density thresholds (Fedorov et al., 2012). The 3D surface meshes obtained for each patient and each control were saved in stl format. Point-to-point distances in the mandible were then measured with Viewbox 4 software (dHalc Software; Fig. S1). It should be noted that only CT scans performed before craniofacial surgery (fronto-facial or fronto-orbital advancement, and posterior vault expansion) were included, in order to avoid potentially confounding effects on mandibular shape.

Western blotting

Cell and brain lysates were subjected to SDS–PAGE on NuPAGE 4–12% bis–tris acrylamide gels (Life Technologies; Thermo Fisher Scientific) and then transferred onto polyvinylidene fluoride membranes. Immunoblotting was performed using standard protocols and the following antibodies: a polyclonal anti-FGFR3 antibody (F0425; 1:1,000 dilution; Sigma-Aldrich), a monoclonal anti-phospho-ERK1/2 antibody (catalog number 4370; 1:1,000 dilution; Cell Signaling), a polyclonal anti-ERK1/2 antibody (M5670; 1:1,000 dilution; Sigma-Aldrich), a monoclonal antibody p44/42 MAPK (catalog number 4696; 1:1,000 dilution; Cell Signaling), a monoclonal anti-phospho-tyrosine P-Tyr-100 antibody (catalog number 9411; 1:1,000 dilution; Cell Signaling), a polyclonal anti-phospho-PLCγ1 antibody (catalog number 2821; 1:1,000 dilution; Cell Signaling), a polyclonal anti-PLCγ1 antibody (catalog number 2822; 1:1,000 dilution; Cell Signaling), a polyclonal anti-phospho-STAT3 antibody (catalog number 9131; 1:1,000 dilution; Cell Signaling), another polyclonal anti-STAT3 antibody (catalog number 9132; 1:1,000 dilution; Cell Signaling), a polyclonal anti-phospho-Akt antibody (catalog number 9271; 1:1,000 dilution; Cell Signaling), a polyclonal anti-Akt antibody (Catalog number 9272; 1:1,000 dilution; Cell Signaling), a polyclonal antibody anti-β-tubulin (catalog number 2146; 1:1,000 dilution; Cell Signaling), and an anti-actin antibody (MAB1501; 1:5,000 dilution; Millipore). Proteins of interest were detected with goat anti-rabbit or anti-mouse secondary antibodies coupled to horseradish peroxidase (1:10,000 dilution; Amersham) and visualized using electrochemiluminescence (RPN2106; Amersham) or (when the Odyssey Li-Cor system was used) with goat anti-mouse IRDye 680RD (925-68070) and goat anti-rabbit IRDye 800CW (925-32211).

Mouse model

All animal studies were performed in accordance with the European Parliament's Directive 2010/63/EU on the protection of animals used for scientific purposes (approval number 27877-2020061712403900). *Fgfr3*$^{A385E/+}$ mice were generated by the Institut Clinique de la Souris (Illkirch, France). A plasmid containing a sequence homologous to exons 5–16 of *Fgfr3* with the 1553GCA>GAA substitution (A385E, exon 9), a neomycin cassette, and Cre recombinase under the control of a Prm1 promoter and flanked by two LoxP sites was stably inserted into BALB/cN mouse embryonic stem cells by homologous recombination. A positive clone was then aggregated into C57BL/6 blastocysts and chimaeras with germline transmission were selected. In the male germline, the cassette was excised using the Prm1 promoter—allowed expression of the *Fgfr3*^{A385E} mutation.

Genotyping

Genomic DNA was isolated from a tail biopsy collected at the age of 7 d via digestion with proteinase K and extraction with

NucleoSpin Tissue reagent, according to the manufacturer's instructions (Macherey-Nagel). Genotypes were determined in two PCR assays; the primers were 5′-GCTTCCCGCTTAAGCGAC AGGTAAC-3′ and 5′-AAAGGGCTAGCTGCTCGGACTTCTATA-3′ in the first assay and 5′-GCTTCCCGCTTAAGCGACAGGTAAC-3′ and 5′-GAAGTTATACTAGAGCGGCCGTTCAC-3′ in the second.

Analysis of the skeletal phenotype

Long bones and body lengths were measured with calipers (VWRi819-0013; VWR International). Whole-skeleton X-rays were acquired using a MX-20 unit (Ultra Focus DXA; Faxitron). µCT datasets were acquired with a SkyScan 1172 scanner (Bruker). For the skull, the acquisition settings were exposure: 100 ms; voltage: 80 kV; current: 100 µA; resolution: 19.9 µm. For the femur, the settings were exposure: 250 ms; voltage: 80 kV; current: 100 µA; resolution: 6.00 µm. Images were reconstructed using NRecon software (Bruker). The reconstructed µCT images of the skull were analyzed using OsiriX 64-bit software (Pixmeo) and those of the femur were analyzed using CTan software (Bruker). For the femur, the bone volume fraction (bone volume/trabecular volume), trabecular thickness, trabecular number, trabecular separation, and the structure model index were measured on a section in the secondary spongiosa. Cortical thickness was measured at midshaft.

Geometric morphometric analysis

We studied mice at the age of 21 d (P21, 9 *Fgfr3*$^{+/+}$ and 8 *Fgfr3*$^{A385E/+}$), 90 d (P90, 10 *Fgfr3*$^{+/+}$ and 8 *Fgfr3*$^{A385E/+}$), and 180 d (P180, 9 *Fgfr3*$^{+/+}$ and 8 *Fgfr3*$^{A385E/+}$). µCT images (acquired as described above) were imported into Avizo 8.1 (Thermo Fisher Scientific) for 3D reconstruction of the skull. A total of 102 anatomic landmarks (most anterior point of the pre-sphenoid, foramen caecum L, foramen caecum R, spheno-ethmoidal synchondrosis L, spheno-ethmoidal synchondrosis R, intra-sphenoidal synchondrosis, on the pre-sphenoid L, intra-sphenoidal synchondrosis, on the pre-sphenoid R, intra-sphenoidal synchondrosis, on the post-sphenoid L, intra-sphenoidal synchondrosis, on the post-sphenoid R, anterior tip of the greater wing of the sphenoid L, anterior tip of the greater wing of the sphenoid R, posterior tip of the greater wing of the sphenoid L, posterior tip of the greater wing of the sphenoid R, spheno-occipital synchondrosis, on the post-sphenoid L, spheno-occipital synchondrosis, on the post-sphenoid R, spheno-occipital synchondrosis, on the basioccipital L, spheno-occipital synchondrosis, on the basioccipital R, mid-point on the anterior margin of the foramen magnum, taken on basioccipital, left anterior intra-occipital synchondrosis, ant. (on the basioccipital), left anterior intra-occipital synchondrosis, post. (on the basioccipital), right anterior intra-occipital synchondrosis, ant. (on the basioccipital), right anterior intra-occipital synchondrosis, post. (on the basioccipital), mid-point on the posterior margin of the foramen magnum, taken on squamous occipital, posterior tip of the otic capsule L, posterior tip of the otic capsule R, inferior concavity of the anterior semi-circular canal L, inferior concavity of the anterior semi-circular canal R, inferior concavity of the lateral semi-circular canal L, inferior concavity of the lateral semi-circular canal R, most anterior point on the ectocranial surface of the squamous occipital, on the suture with the interparietal, paracondylar process L, paracondylar process R, root of the zygoma, greater concavity L, root of the zygoma, greater concavity R, posterior end of the metopic suture (midline), head of the malleus L, tip of the manubrium of the malleus L, head of the malleus R, tip of the manubrium of the malleus R, posterior tip of the squamosal L, greater concavity of the posterior indentation of the squamosal L, posterior tip of the squamosal R, greater concavity of the posterior indentation of the squamosal R, inferior tip of the coronal suture L, inferior tip of the coronal suture R, posterior concavity of the emergence of the V1 nerve L, posterior concavity of the emergence of the V1 nerve R, frontosphenoidal suture at the border of the optic canal L (on the frontal), frontosphenoidal suture at the border of the optic canal R (on the frontal), posterior tip of the mandibular condyle L, anterior tip of the mandibular condyle L, tip of the coronoid process L, greater concavity of the sigmoid notch L, tip of the mandibular angle L, greater concavity of the ramus L, anterior tip of the external oblique line L, masseter insertion ant. L, masseter insertion post. L, molar alveolar mandible L, molar alveolar maxilla L, mandibular incisor greater inferior concavity L, mandibular incisor superior ridge L, posterior tip of the mandibular condyle R, anterior tip of the mandibular condyle R, tip of the coronoid process R, greater concavity of the sigmoid notch R, tip of the mandibular angle R, greater concavity of the ramus R, anterior tip of the external oblique line R, masseter insertion ant. R, masseter insertion post. R, molar alveolar mandible R, molar alveolar maxilla R, mandibular incisor greater inferior concavity R, mandibular incisor superior ridge R, anterolateral corner of the nasal bone L, anterolateral corner of the nasal bone R, anteromedial corner of the nasal bone L, anteromedial corner of the nasal bone R, posterolateral corner of the nasal bone L, posterolateral corner of the nasal bone R, posteromedial corner of the nasal bone L, posteromedial corner of the nasal bone R, temporozygomatic suture post. L (on the zygoma), temporozygomatic suture ant. L (on the zygoma), maxillozygomatic suture post. L (on the maxilla), maxillozygomatic suture ant. L (on the maxilla), temporozygomatic suture post. R (on the zygoma), temporozygomatic suture ant. R (on the zygoma), maxillozygomatic suture post. R (on the maxilla), maxillozygomatic suture ant. R (on the maxilla), V2 foramen, maximum post. concavity L, V2 foramen, maximum post. concavity R, V2 foramen, maximum ant. concavity L, V2 foramen, maximum ant. concavity R, frontomaxillary suture, posterior tip L (on the maxilla), frontomaxillary suture, posterior tip R (on the maxilla), anterior palatine foramen ant. concavity L, anterior palatine foramen ant. concavity R, anterior palatine foramen post. concavity L, anterior palatine foramen post. concavity R, maxillopremaxillary suture (midline, on the permaxilla), palatomaxillary suture, lat. L (on the palatine), palatomaxillary suture, lat. R (on the palatine), most posterior tip of the medial pterygoid process L, most posterior tip of the medial pterygoid process R, posterior choana, antero-lateral corner L, posterior choana, antero-lateral corner R) were then positioned on the skull and exported into MorphoJ (Klingenberg, 2011) for geometric morphometric analysis, including Procrustes superimposition and the computation of mean models for each age group and each genotype. The Procrustes distances (*d*) separating groups in the morphospace were computed, and significance was assessed in permutation tests (10,000 rounds). We considered that a significant value of *d* corresponded to a significant intergroup difference in shape. Shape

differences were visualized by projecting heat maps onto the 3D skull or mandible, using Avizo 8.1 (Thermo Fisher Scientific).

Tissue histology and immunohistology

Brains

Mice were anesthetized with an intraperitoneal injection of ketamine/xylazine and perfused transcardially with cold PBS and then cold 4% paraformaldehyde (PFA). The brains were dissected out and postfixed overnight in 4% PFA solution at 4°C. Serial coronal floating sections (30 µm) were obtained using a VT1000S vibratome (Leica). For immunofluorescence staining, slides were labeled with polyclonal antibodies against FGFR3 (catalog number F0425; 1:250 dilution; Sigma-Aldrich) and NeuN (catalog number 26975-1-AP; 1:250 dilution; Proteintech). The slides were washed and incubated with Alexa Fluor 594 donkey anti-rabbit IgG (R37119; 1:2,000 dilution; Life Technologies). Slides were mounted using DAPI-Fluoromount-G (SouthernBiotech) containing DAPI for nuclear staining. Doublecortin was immunolabeled (polyclonal antibody; #SC 8066; 1:500 dilution; Santa Cruz) as described previously (Denny et al., 2012). A terminal deoxynucleotidyl transferase dUTP nick end labeling (TUNEL) assay was performed using an ApopTagPeroxidase in situ apoptosis detection kit (Millipore), according to the manufacturer's instructions.

Skin

Human and mouse skin samples were fixed in overnight in 4% PFA solution at 4°C. Serial 5 µm sections were prepared and stained with hematoxylin–eosin reagent. Slides were labeled with a polyclonal antibody against FGFR3 (catalog number F0425; 1:250 dilution; Sigma-Aldrich) and a monoclonal antibody against phospho-ERK1/2 (catalog number 4370; 1:500 dilution; Cell Signaling).

Cochlear cryosections

For cochlear samples, P3 temporal bones (n = 1 for the WT, n = 2 for the mutant) were dissected and fixed at room temperature for 2 h or at 4°C overnight and then decalcified overnight at 4°C in a solution of 10% EDTA/PBS. The samples were then embedded in sucrose/gelatin, as described elsewhere (Mansour et al., 2013). Sections (thickness: 14 µm) prepared in the modiolar plane were stained with the following primary antibodies: rat anti-CD44 (550538; 1:1,000; BD Biosciences), rabbit anti-MYO7A (25-6790; 1:1,000; Proteus Biosciences), rabbit anti-p75NTR (#07-476; 1:650; Millipore), or goat anti-PROX1 (AF2727; 1:200; R&D Systems). The secondary antibodies were Alexa Fluor 594 goat anti-rat (A11007; 1:400; Invitrogen), Alexa Fluor 488 goat anti-rabbit (A11034; 1:400; Invitrogen), or Alexa Fluor 488 donkey anti-goat (A11055; 1:400; Invitrogen). DAPI was included in the mounting medium (Vectashield; Vector Labs).

Microscopy image acquisition and quantification

Bright-field images were captured with a PD70-IX2-UCB microscope and CellSens software (Olympus). Fluorescence images were obtained using a Yokogawa CSU-X1 spinning disk scanner coupled to a Zeiss Observer Z1 inverted microscope and controlled with Zen Blue software (Carl Zeiss). Zen Blue software (Carl Zeiss) was used to count cells and measure surface areas. For the quantification of immunofluorescence signals in the brain, the values for six successive slices in each hemisphere and each individual were averaged.

Brain MRI

The mice underwent brain MRI at the Small Animal Imaging Facility at Université Paris Descartes Sorbonne Paris Cité's Faculty of Medicine (Paris, France), using a small-animal 4.7-T unit (Biospec 47/40; Bruker) with a resolution of 100 µm. Mice were anesthetized with isoflurane gas inhalation during the acquisition. Measurements were taken with ImageJ software.

Osteoblast culture

Primary osteoblasts from mouse calvaria were obtained by sequential collagenase type IV digestion of 2- to 3-d-old pup calvaria. The cells were expanded in T25 flasks to subconfluence in Minimum Essential Medium Alpha (Life Technologies) supplemented with 10% fetal bovine serum, 2 mM glutamine, 100 U/ml penicillin, and 100 µg/ml streptomycin and then harvested with trypsin/EDTA (Life Technologies). For mineralization studies, cells were plated in 24-well plates (25,000 cells/well) and cultured for up to 21 d in differentiation medium with 50 mg/ml ascorbic acid and 10 mM glycerol-2-phosphate di-sodium salt hydrate (Sigma-Aldrich). Alkaline phosphatase activity was assayed by fixing cells in cold 4% PFA and incubating them with 1-Step NBT/BCIP Substrate Solution (Thermo Fisher Scientific). Mineralization activity was assayed by fixing cells in cold 4% PFA and incubating them with 2% Alizarin red solution (Sigma-Aldrich). Cell density was assessed by fixing cells in cold methanol and incubating them with 0.5% crystal violet/25% methanol solution. The alizarin red and crystal violet colorations were then resuspended in DMSO, and absorbance was measured at 570 nm (for Alizarin) or 410 nm (for alkaline phosphatase [ALP]).

For protein lysate experiments, cells were plated in 6-well plates (200,000 cells/well) and cultured for up to 21 d in differentiation medium. The cells were depleted overnight, treated with 100 ng/ml Fibroblast Growth Factor 2 (Fgf2; Peprotech) for 5 min, and lysed in radioimmunoprecipitation assay lysis buffer.

For proliferation assays, cells were plated in 96-well plates (1,000 cells/well), cultured in differentiation medium, and recorded for 7 d using an Incucyte Live-Cell Analysis System. Each well was imaged every 3 h.

Generation of human cDNA FGFR3^{A391E} constructs

Full-length human FGFR3 cDNA was purchased from Origene Technologies, Inc. Sequence fragments of 624 bp of the gene containing the A391E mutation and localized between unique restriction sites for CpoI and MluI enzymes were generated by Eurofins Genomics. Full-length FGFR3 cDNA and sequence fragments were digested using CpoI (Anza 63 CpoI Enzyme; Thermo Fisher Scientific) and MluI (Anza 28 MluI Enzyme; Thermo Fisher Scientific), according to the manufacturer's instructions. Digested fragments were separated on an agarose gel and purified with NucleoSpin gel and a PCR clean-up kit

(Macherey-Nagel). Full-length cDNA containing the A391E mutation was then assembled using a T4 ligation kit and amplified into MAX Efficiency DH5α–competent cells (Thermo Fisher Scientific). All cDNA sequences were checked by Sanger sequencing.

Transient transfections using FGFR3 cDNA constructs

Human embryonic kidney cells were cultured in 6-well plates and transiently transfected at 80% confluence with human FGFR3 constructs (FGFR3 and FGFR3^{A391E}) using JetPrime (Polyplus-transfection), according to the manufacturer's instructions. Cells were then depleted overnight and treated with Fgf2 100 ng/ml (Catalog Number: AF-100-18B; Peprotech) for 5 min, or after depletion, cells were treated overnight with 100 nM BGJ398 (LC Laboratories). Transfected cells were then lysed in radioimmunoprecipitation assay buffer (50 mM Tris-HCl pH 7.6, 150 mM NaCl, 0.5% NP40, and 0.25% sodium deoxycholate, supplemented with protease and phosphatase inhibitors; Roche). Immunoprecipitation was performed by overnight incubation at 4°C with 3 µl anti-FGFR3 (F0425; Sigma-Aldrich) per 60 µg protein and then hybridization with protein A–agarose (Roche).

Sanger sequencing

RNA from osteoblasts and brain was extracted using an RNeasy Kit (Qiagen) and then reverse transcriptase using SuperScript III Reverse Transcriptase (Thermo Fisher Scientific). The PCR products were amplified using GoTaq DNA polymerase (Promega) and the primer pair 5′-GGAGGAGCTGATGGAAACTG-3′ and 5′-AACATTGGCCAGAACAGGAC-3′ and then sequenced using a BigDye Terminator v3.1 cycle sequencing kit (Thermo Fisher Scientific), according to the manufacturer's instructions. Sequences were analyzed using DNADynamo software (Blue Tractor Software Ltd).

Surgery and drug treatment

BGJ398 was purchased from LC Laboratories. 4-mo-old *Fgfr3*$^{A385E/+}$ mice received daily ICV injections of BGJ398 (1 µg per injection) or vehicle (artificial cerebrospinal fluid with DMSO 5%) for 7 d. The last injection was performed 1 h before behavioral testing. For systemic administration, the mice received daily intraperitoneal injections of BGJ398 (2 mg/kg in DMSO 2%) or vehicle (artificial cerebrospinal fluid with DMSO 2%) for 7 d. The last injection was performed 1 h before behavioral testing.

ICV cannula implantation

Mice were anesthetized with an intraperitoneal injection of ketamine hydrochloride (20 mg/kg; Virbac) and xylazine (100 mg/kg body weight; Rompun 2%; Bayer) and placed in a stereotaxic frame (900SL; Kopf Instruments). To prevent desiccation during surgery, an ophthalmic eye ointment was applied to the cornea. The area around the incision was trimmed, and Vetoquinol was applied. After exposure of the dorsal skull, a hole was made at the following coordinates: anterior-posterior −0.5, medial-lateral −1.0 (in mm, from the bregma). A guide cannula (C235GS; 26 gauge; Plastics One) with a dummy cannula (C235DCS; Plastics One) was inserted through the hole into the brain ventricle and secured to the skull with dental cement (Super-Bond C&B; Sun Medical). Lastly, the scalp incision was sutured around the cannula, and the mouse was observed in a recovery chamber until it was fully mobile.

Drug preparation and infusion

For intraperitoneal injections, BGJ398 was dissolved to a concentration of 4 mg/ml in artificial cerebrospinal fluid. Mice received a daily intraperitoneal injection for 7 d.

For ICV infusion, BGJ398 was dissolved to a concentration of 0.66 µg/µl in artificial cerebrospinal fluid. Every day for 7 d, the experimenter gently restrained the mouse and then replaced a dummy cannula with an ICV injector cannula (C235IS; 33 gauge, extending 0.5 mm beyond the 1.5 mm guide cannula). The drug was infused (1.0 µl/side, at a rate of 1 µl/min) using a syringe pump (Harvard Apparatus) and a 10 µl Hamilton syringe connected to the injector cannula. After the infusion, the injector was replaced by the dummy cannula.

Behavioral tests

Three-foot shock CFC

Mice were transported to the testing room (a short distance from the mouse holding facility) in their home cages and left undisturbed for at least one hour before the beginning of the test. The conditioning chambers (internal dimensions: 25 × 25 × 25 cm) were purchased from Bioseb (Vitrolles, France). Each chamber was located inside a larger, insulated plastic cabinet that provided protection from outside light and noise (67 × 55 × 50 cm; Bioseb). Mice were tested individually in the conditioning boxes. The floor of the chamber consisted of 27 stainless steel bars wired to a shock generator with a scrambler for the delivery of a foot shock. The signal generated by the mouse's movements was recorded and analyzed using a high-sensitivity weight transducer system. The analog signal was transmitted to the freezing software module through the load cell unit. The ratio between time active and time immobile (freezing) was determined and analyzed. The CFC procedure took place over 2 d consecutively. On day 1, the mice received a foot shock (1.5 s, 0.5 mA) 60, 120, and 180 s after being placed in the conditioning chamber. The mice were returned to their home cages 60 s after the last shock. Contextual fear memory was assessed 24 h after conditioning by returning the mice to the conditioning chamber and measuring freezing behavior during a 4-min retention test. Freezing (defined as immobility for at least 2 s) was scored automatically and analyzed using Packwin 2.0 software (Bioseb). The results were checked by two observers (M. Cornille and S. Moriceau) blinded to the mouse's treatment group.

The NOR test

We used a modified version of the NOR test described by Glatigny et al. (2019). Mice were transported to the testing room (a short distance from the mouse holding facility) in their home cages and left undisturbed for at least one hour before the beginning of the test. The testing room was lit with two 60 W light bulbs, and test sessions were recorded with a camera placed above the test arena (a grey plastic box, 60 × 40 × 32 cm). The mice could not contact or see each other during the exposures.

The light intensity was equal in all parts of the arena (~20 lx). Two different objects (available in triplicate) were used: a blue ceramic pot (diameter: 6.5 cm; maximum height: 7.5 cm; object A) and a clear, plastic funnel (diameter: 8.5 cm; maximum height: 8.5 cm; object B). In pilot experiments and the training phase, the two objects elicited equal levels of exploration. The object that served as the novel object and the left or right placement of the objects were counterbalanced within each group. Between exposures, mice were held individually in standard cages, the objects and arenas were cleaned with a sporicidal disinfectant (Phagosphore; Christeyns), and the bedding was replaced.

The NOR paradigm (over 3 d) consists of a habituation phase, a training phase, and a testing phase. Mice were always placed in the center of the arena at the start of each exposure. On day 1 (the habituation phase), mice were given 5 min to explore the object-free arena and were then returned to their home cage. On day 2 (the training phase), mice were allowed to explore two identical objects (arranged in a symmetric position opposite to the center of the arena) for 10 min and were then returned to their home cage. On day 3 (the testing phase), mice were given 15 min to explore a familiar object and a novel object in the same arena and in the same positions as in the training phase. The following behaviors were scored as exploration: sniffing, licking, touching the object with the nose or with the front legs, or proximity (≤1 cm) between the nose and the object. If the mouse was on top of the object or was completely immobile, exploration was not scored. The preference index for the novel object was calculated as (time spent exploring the new object/the total time spent exploring both objects), and the discrimination index was calculated as (time spent exploring the new object – time spent exploring the familiar object)/(total time spent exploring both objects). As a control, the preference index for the (right/left) object location or for object A versus B during the training phase was measured in all tested groups of mice. We confirmed that none of the groups had an initial preference for one or other of the exposed objects or a right/left orientation. Locomotion was assessed for each mouse. Behavior was scored on video by two observers (M. Cornille and S. Moriceau), who were blinded to the mice's treatment group. The total object exploration time was quantified in the training and testing phases.

The NOL test

In the NOL task, all procedures were the same as in the NOR task, except that mice encountered two familiar objects (rather than one familiar object and one novel object) during the testing phase. However, one of the familiar objects was located in a new position in the arena. The duration and frequency of exploration of the relocated object constituted indices of memory performance. As a control, the preference index for the (right/left) object location during the NOL training phase was measured in all groups of mice. We confirmed that none of the groups had an initial preference for a right/left orientation. Behavior was scored on video by two observers (M. Cornille and S. Moriceau), who were blinded to the mice's treatment group. The total object exploration time was quantified in the training and testing phases.

The light/dark transition test

This test is based on rodents' innate aversion to brightly illuminated areas and on their spontaneous exploratory behavior in response to the stressor that light represents. The test apparatus consisted of a dark, safe compartment and an aversive compartment illuminated with an 8 W fluorescent tube (1,000 lx). Naive mice were placed individually in the middle of the testing chamber's dark compartment, facing away from the doorway to the light compartment. Mice were tested for 10 min, and two indices of anxiety-related behavior and exploratory activity were recorded: time spent in the lit compartment and the number of transitions between compartments. Behavior was scored using an infrared light beam activity monitor and actiMot2 software (TSE Systems; Bad Homburg vor der Höhe) and analyzed using GraphPad Prism statistics software (version 5; GraphPad Software, Inc.).

The OFT

This test also takes advantage of rodents' aversion to brightly lit areas. Each mouse was placed in the center of the OFT chamber (43 × 43 cm) and was allowed to explore for 30 min. Mice were monitored throughout each test session with an infrared light beam activity monitor and actiMot2 Software (TSE Systems). Overall motor activity was quantified as the total distance travelled (ambulation). Anxiety was quantified by measuring the time and distance spent in the center versus the periphery of the OFT chamber.

The MWM

Mice were transported to the testing room (a short distance from the mouse holding facility) in their home cages and left undisturbed for at least one hour before the beginning of the test. A MWM with an automatic tracking system was used to assess spatial learning and memory. The apparatus was a white circular swimming pool (diameter: 200 cm, walls: 60 cm high) located in a room with various distal cues. The pool was filled with water (depth: 50 cm) maintained at 22 ± 1°C. The water was made opaque by the addition of a nontoxic white paint. A 12-cm round platform was hidden 1.0 cm below the water surface. The maze was virtually divided into four arbitrary, equally spaced quadrants delineated by the cardinal points north, east, south, and west. The pool was located in a brightly lit room. Extra-maze geometric, high-contrast cues were mounted on the walls of the swimming pool, with the ceiling providing illumination. Data were collected using a video camera fixed to the ceiling and connected to a video-tracking system (Anymaze; Stoelting Co.). Each daily session consisted of four swimming trials, in which each mouse was placed in the pool facing the wall of the tank; the animal had to swim to the platform within 120 s. A trial terminated when the animal reached the platform and remained there for 5 s. Mice were removed and placed back in their home cages during a 5 min intertrial interval. To prevent hypothermia, the animals were gently dried with a paper towel between and after the trials. The starting point differed for each trial, and the release point sequences differed from one day to the next. The animal's movements were recorded using Anymaze, and the time spent swimming to the platform was calculated as an index of memory performance.

Memory-related stimulation procedures

Animals were exposed to CFC to induce memory-related stimulations. For the CFC, the training phase lasted 4 d. Mice were placed in the conditioning chamber and received three shocks at 60, 120, and 180 s (1 s, 0.3 mA). The animals were removed 60 s after the last shock and returned to their home cages. This procedure was repeated four times. Contextual fear memory was assessed 24 h after the training by returning the mice to the same conditioning chamber and measuring the freezing behavior during a 4 min retention test. On the last day of stimulation, the mice were sacrificed 1 h after the last exposure to the CFC task.

Golgi-Cox staining and dendritic spine quantification

4-mo-old treated mice were perfused intracardially with 4% PFA, and the isolated brains were impregnated with an FD Rapid GolgiStain kit (FD Neuro Technologies) according to the manufacturer's instructions. Bright field z stacks of 150 µm sections were obtained using a Zeiss Apotome2 (40× objective). Dendritic spine density was quantified manually, using Fiji ImageJ software. For each group of mice, five secondary dendrite segments from 20 to 30 DG granular layer cells were quantified. The investigator who rated the dendritic spine density was blinded to the sample's origin.

Statistical analysis

Quantitative variables were described as the mean ± SEM. Statistical parameters (including the sample size [*n*], the post hoc test used, and the statistical significance) are reported in the figures and their legends. Groups were compared in a nonparametric Mann–Whitney *U* test, Student's *t* test, or a one-way ANOVA, as appropriate. If a one-way ANOVA revealed a statistically significant difference between groups of mice, it was followed by a two-way repeated-measures ANOVA and Tukey's post-hoc test for multiple comparisons. The threshold for statistical significance was set to $P \leq 0.05$. All statistical analyses were performed using GraphPad Prism software (version 5; GraphPad Software, Inc.).

Online supplemental material

Fig. S1 shows craniofacial features of CAN patients and mandible measurements (body length, ramus height, intergonial distance, condylar length, and condylar width). HES and FGFR3 and phosphorylated Erk1/2 immunostaining paraffin sections of healthy skin and acanthosis nigricans areas from patient. Fig. S2 shows ALP activity and alizarin red staining of mouse calvarial osteoblasts, osteoblast proliferation and phosphorylated Erk1/2 expression, µCT scan of the femur of mutant mice and control. histological analysis of mouse skin, and inner ear analysis. Fig. S3 shows hippocampus heterozygous CAN mutations, NOL discrimination index, NOR exploratory of left object, latency to find the platform during MWM test, NOL and NOR test training phase, and TUNEL experiments.

Acknowledgments

We thank the Imagine Institute's imaging facility and the Structure Federative de Recherche's histology facility for their help with this work. We are grateful to the families who participated in this study.

This research program received a state subsidy managed by the French National Research Agency as part of the "Investments for the Future" program (reference: ANR-10-IAHU-01). L. Legeai-Mallet is funded by AXA-Imagine Head-Heart Chair. F. Oury is funded by the Fondation pour la Recherche Médicale and the AGEMED-INSERM program. S. Moriceau received a grant from the National Institutes of Health (R01 DC014470). For generation of the mouse model, L. Legeai-Mallet was funded by the Fondation Maladies Rares.

Author contributions: L. Legeai-Mallet conceived the project. L. Legeai-Mallet and F. Oury designed the research. M. Cornille and S. Moriceau performed the behavioral experiments. M. Cornille, Y. Heuzé, R.H. Khonsari, A. Morice, V. Boitez, and M. Bensidhoum performed and analyzed morphometric and geometric analyses. C. Collet performed the genetic analyses. S. Moriceau interpreted the cochlear data. T. Rauschendorfer and S. Werner interpreted the skin data. G. Paternoster, E. Arnaud, and N. Boddaert analyzed the human MRI data. L. Loisay and V. Boitez performed the WB analyses. M. Cornille and S. Moriceau prepared the figures. L. Legeai-Mallet, F. Oury, M. Cornille, S. Moriceau, and F. Di Rocco wrote the manuscript, and all other authors provided critical comments on the manuscript. All authors read and approved the final manuscript.

Disclosures: L. Legeai-Mallet and F. Oury reported a patent to BIO19248 pending. No other disclosures were reported.

Submitted: 1 September 2020
Revised: 9 June 2021
Accepted: 13 January 2022

References

Aldridge, K., C.A. Hill, J.R. Austin, C. Percival, N. Martinez-Abadias, T. Neuberger, Y. Wang, E.W. Jabs, and J.T. Richtsmeier. 2010. Brain phenotypes in two FGFR2 mouse models for Apert syndrome. *Dev. Dyn.* 239:987–997. https://doi.org/10.1002/dvdy.22218

Al-Namnam, N.M., F. Hariri, M.K. Thong, and Z.A. Rahman. 2019. Crouzon syndrome: Genetic and intervention review. *J. Oral Biol. Craniofac. Res.* 9:37–39. https://doi.org/10.1016/j.jobcr.2018.08.007

Arnaud-López, L., R. Fragoso, J. Mantilla-Capacho, and P. Barros-Núñez. 2007. Crouzon with acanthosis nigricans. Further delineation of the syndrome. *Clin. Genet.* 72:405–410. https://doi.org/10.1111/j.1399-0004.2007.00884.x

Bansal, R., V. Lakhina, R. Remedios, and S. Tole. 2003. Expression of FGF receptors 1, 2, 3 in the embryonic and postnatal mouse brain compared with Pdgfralpha, Olig2 and Plp/dm20: Implications for oligodendrocyte development. *Dev. Neurosci.* 25:83–95. https://doi.org/72258

Chen, F., C. Degnin, M. Laederich, W.A. Horton, and K. Hristova. 2011. The A391E mutation enhances FGFR3 activation in the absence of ligand. *Biochim. Biophys. Acta*. 1808:2045–2050. https://doi.org/10.1016/j.bbamem.2011.04.007

Chen, F., S. Sarabipour, and K. Hristova. 2013. Multiple consequences of a single amino acid pathogenic RTK mutation: The A391E mutation in FGFR3. *PLoS One*. 8:e56521. https://doi.org/10.1371/journal.pone.0056521

Coll, G., J.-J. Lemaire, F. Di Rocco, I. Barthélémy, J.-M. Garcier, E. De Schlichting, and L. Sakka. 2016. Human foramen magnum area and posterior cranial fossa volume growth in relation to cranial base synchondrosis closure in the course of child development. *Neurosurgery*. 79:722–735. https://doi.org/10.1227/NEU.0000000000001309

Coll, G., L. Sakka, C. Botella, N. Pham-Dang, C. Collet, M. Zerah, E. Arnaud, and F. Di Rocco. 2018. Pattern of closure of skull base synchondroses in

Crouzon syndrome. *World Neurosurg.* 109:e460–e467. https://doi.org/10.1016/j.wneu.2017.09.208

Colvin, J.S., B.A. Bohne, G.W. Harding, D.G. McEwen, and D.M. Ornitz. 1996. Skeletal overgrowth and deafness in mice lacking fibroblast growth factor receptor 3. *Nat. Genet.* 12:390–397. https://doi.org/10.1038/ng0496-390

Cornille, M., E. Dambroise, D. Komla-Ebri, N. Kaci, M. Biosse-Duplan, F. Di Rocco, and L. Legeai-Mallet. 2019. Animal models of craniosynostosis. *Neurochirurgie.* 65:202–209. https://doi.org/10.1016/j.neuchi.2019.09.010

Dabrowski, A., A. Terauchi, C. Strong, and H. Umemori. 2015. Distinct sets of FGF receptors sculpt excitatory and inhibitory synaptogenesis. *Development.* 142:1818–1830. https://doi.org/10.1242/dev.115568

Dambroise, E., I. Ktorza, A. Brombin, G. Abdessalem, J. Edouard, M. Luka, I. Fiedler, O. Binder, O. Pelle, E.E. Patton, et al. 2020. Fgfr3 is a positive regulator of osteoblast expansion and differentiation during zebrafish skull vault development. *J. Bone Miner. Res.* 35:1782–1797. https://doi.org/10.1002/jbmr.4042

Deng, C., A. Wynshaw-Boris, F. Zhou, A. Kuo, and P. Leder. 1996. Fibroblast growth factor receptor 3 is a negative regulator of bone growth. *Cell.* 84:911–921. https://doi.org/10.1016/s0092-8674(00)81069-7

Denny, C.A., N.S. Burghardt, D.M. Schachter, R. Hen, and M.R. Drew. 2012. 4- to 6-week-old adult-born hippocampal neurons influence novelty-evoked exploration and contextual fear conditioning. *Hippocampus.* 22:1188–1201. https://doi.org/10.1002/hipo.20964

Di Rocco, F., C. Collet, L. Legeai-Mallet, E. Arnaud, M. Le Merrer, S. Hadj-Rabia, and D. Renier. 2011. Crouzon syndrome with acanthosis nigricans: A case-based update. *Childs Nerv Syst.* 27:349–354. https://doi.org/10.1007/s00381-010-1347-z

Ennaceur, A., and J. Delacour. 1988. A new one-trial test for neurobiological studies of memory in rats. 1: Behavioral data. *Behav. Brain Res.* 31:47–59. https://doi.org/10.1016/0166-4328(88)90157-x

Fedorov, A., R. Beichel, J. Kalpathy-Cramer, J. Finet, J.-C. Fillion-Robin, S. Pujol, C. Bauer, D. Jennings, F. Fennessy, M. Sonka, et al. 2012. 3D slicer as an image computing platform for the quantitative imaging network. *Magn. Reson. Imaging.* 30:1323–1341. https://doi.org/10.1016/j.mri.2012.05.001

Glatigny, M., S. Moriceau, M. Rivagorda, M. Ramos-Brossier, A.C. Nascimbeni, F. Lante, M.R. Shanley, N. Boudarene, A. Rousseaud, A.K. Friedman, et al. 2019. Autophagy is required for memory formation and reverses age-related memory decline. *Curr. Biol.* 29:435–448.e8. https://doi.org/10.1016/j.cub.2018.12.021

Grosso, S., M.A. Farnetani, R. Berardi, G. Bartalini, M. Carpentieri, P. Galluzzi, R. Mostardini, G. Morgese, and P. Balestri. 2003. Medial temporal lobe dysgenesis in Muenke syndrome and hypochondroplasia. *Am. J.Med. Genet.A.* 120A:88–91. https://doi.org/10.1002/ajmg.a.10171

Gudernova, I., I. Vesela, L. Balek, M. Buchtova, H. Dosedelova, M. Kunova, J. Pivnicka, I. Jelinkova, L. Roubalova, A. Kozubik, and P. Krejci. 2016. Multikinase activity of fibroblast growth factor receptor (FGFR) inhibitors SU5402, PD173074, AZD1480, AZD4547 and BGJ398 compromises the use of small chemicals targeting FGFR catalytic activity for therapy of short stature syndromes. *Hum. Mol. Genet.* 25:9–23. https://doi.org/10.1093/hmg/ddv441

Gürbüz, F., S. Ceylaner, A.K. Topaloğlu, and B. Yüksel. 2016. Crouzonodermoskeletal syndrome with hypoplasia of corpus callosum and inferior vermis. *J. Clin. Res. Pediatr. Endocrinol.* 8:373–374. https://doi.org/10.4274/jcrpe.3343

Heuzé, Y., S.A. Boyadjiev, J.L. Marsh, A.A. Kane, E. Cherkez, J.E. Boggan, and J.T. Richtsmeier. 2010. New insights into the relationship between suture closure and craniofacial dysmorphology in sagittal nonsyndromic craniosynostosis. *J. Anat.* 217:85–96. https://doi.org/10.1111/j.1469-7580.2010.01258.x

Inglis-Broadgate, S.L., R.E. Thomson, F. Pellicano, M.A. Tartaglia, C.C. Pontikis, J.D. Cooper, and T. Iwata. 2005. FGFR3 regulates brain size by controlling progenitor cell proliferation and apoptosis during embryonic development. *Developmental Biol.* 279:73–85. https://doi.org/10.1016/j.ydbio.2004.11.035

Itoh, K., R. Pooh, Y. Kanemura, M. Yamasaki, and S. Fushiki. 2013. Brain malformation with loss of normal FGFR3 expression in thanatophoric dysplasia type I. *Neuropathology.* 33:663–666. https://doi.org/10.1111/neup.12036

Iwata, T., and R.F. Hevner. 2009. Fibroblast growth factor signaling in development of the cerebral cortex. *Dev. Growth Differ.* 51:299–323. https://doi.org/10.1111/j.1440-169X.2009.01104.x

Kitamura, T., and K. Inokuchi. 2014. Role of adult neurogenesis in hippocampal-cortical memory consolidation. *Mol. Brain.* 7:13. https://doi.org/10.1186/1756-6606-7-13

Klingenberg, C.P. 2011. MorphoJ: An integrated software package for geometric morphometrics. *Mol. Ecol. Resour.* 11:353–357. https://doi.org/10.1111/j.1755-0998.2010.02924.x

Komla-Ebri, D., E. Dambroise, I. Kramer, C. Benoist-Lasselin, N. Kaci, C. Le Gall, L. Martin, P. Busca, F. Barbault, D. Graus-Porta, et al. 2016. Tyrosine kinase inhibitor NVP-BGJ398 functionally improves FGFR3-related dwarfism in mouse model. *J. Clin. Invest.* 126:1871–1884. https://doi.org/10.1172/JCI83926

Kruszka, P., Y.A. Addissie, N.B. Agochukwu, E.S. Doherty, and M. Muenke. 1993. Muenke syndrome. In GeneReviews. M.P. Adam, H.H. Ardinger, R.A. Pagon, S.E. Wallace, L.J. Bean, K. Stephens, A. Amemiya, editors. University of Washington, Seattle, WA.

Laurita, J., E. Koyama, B. Chin, J.A. Taylor, G.E. Lakin, K.D. Hankenson, S.P. Bartlett, and H.-D. Nah. 2011. The Muenke syndrome mutation (FgfR3P244R) causes cranial base shortening associated with growth plate dysfunction and premature perichondrial ossification in murine basicranial synchondroses. *Dev. Dyn.* 240:2584–2596. https://doi.org/10.1002/dvdy.22752

Levenga, J., H. Wong, R.A. Milstead, B.N. Keller, L.E. Laplante, and C.A. Hoeffer. 2017. AKT isoforms have distinct hippocampal expression and roles in synaptic plasticity. *bioRxiv*:168336. https://doi.org/10.1101/168336

Li, E., M. You, and K. Hristova. 2006. FGFR3 dimer stabilization due to a single amino acid pathogenic mutation. *J. Mol. Biol.* 356:600–612. https://doi.org/10.1016/j.jmb.2005.11.077

Maliepaard, M., I.M.J. Mathijssen, J. Oosterlaan, and J.M.E. Okkerse. 2014. Intellectual, behavioral, and emotional functioning in children with syndromic craniosynostosis. *Pediatrics.* 133:e1608–e1615. https://doi.org/10.1542/peds.2013-3077

Mansour, S.L., C. Li, and L.D. Urness. 2013. Genetic rescue of Muenke syndrome model hearing loss reveals prolonged FGF-dependent plasticity in cochlear supporting cell fates. *Genes Dev.* 27:2320–2331. https://doi.org/10.1101/gad.228957.113

Martínez-Abadías, N., Y. Heuzé, Y. Wang, E.W. Jabs, K. Aldridge, and J.T. Richtsmeier. 2011. FGF/FGFR signaling coordinates skull development by modulating magnitude of morphological integration: Evidence from apert syndrome mouse models. *PLoS One.* 6:e26425. https://doi.org/10.1371/journal.pone.0026425

Meyers, G.A., S.J. Orlow, I.R. Munro, K.A. Przylepa, and E.W. Jabs. 1995. Fibroblast growth factor receptor 3 (FGFR3) transmembrane mutation in Crouzon syndrome with acanthosis nigricans. *Nat. Genet.* 11:462–464. https://doi.org/10.1038/ng1295-462

Minatohara, K., M. Akiyoshi, and H. Okuno. 2015. Role of immediate-early genes in synaptic plasticity and neuronal ensembles underlying the memory trace. *Front Mol. Neurosci.* 8:78. https://doi.org/10.3389/fnmol.2015.00078

Moldrich, R.X., C. Mezzera, W.M. Holmes, S. Goda, S.J. Brookfield, A.J. Rankin, E. Barr, N. Kurniawan, D. Dewar, L.J. Richards, et al. 2011. Fgfr3 regulates development of the caudal telencephalon. *Dev. Dynam.* 240:1586–1599. https://doi.org/10.1002/dvdy.22636

Morice, A., R. Cornette, A. Giudice, C. Collet, G. Paternoster, É. Arnaud, E. Galliani, A. Picard, L. Legeai-Mallet, and R.H. Khonsari. 2020. Early mandibular morphological differences in patients with FGFR2 and FGFR3-related syndromic craniosynostoses: A 3D comparative study. *Bone.* 141:115600. https://doi.org/10.1016/j.bone.2020.115600

Müller Smith, K., D.M. Fagel, H.E. Stevens, R.L. Rabenstein, M.E. Maragnoli, Y. Ohkubo, M.R. Picciotto, M.L. Schwartz, and F.M. Vaccarino. 2008. Deficiency in inhibitory cortical interneurons associates with hyperactivity in fibroblast growth factor receptor 1 mutant mice. *Biol. Psychiatry.* 63:953–962. https://doi.org/10.1016/j.biopsych.2007.09.020

Oh, L.Y.S., A. Denninger, J.S. Colvin, A. Vyas, S. Tole, D.M. Ornitz, and R. Bansal. 2003. Fibroblast growth factor receptor 3 signaling regulates the onset of oligodendrocyte terminal differentiation. *J. Neurosci.* 23:883–894. https://doi.org/10.1523/JNEUROSCI.23-03-00883.2003

Ohkubo, Y., A.O. Uchida, D. Shin, J. Partanen, and F.M. Vaccarino. 2004. Fibroblast growth factor receptor 1 is required for the proliferation of hippocampal progenitor cells and for hippocampal growth in mouse. *J. Neurosci.* 24:6057–6069. https://doi.org/10.1523/JNEUROSCI.1140-04.2004

Okubo, Y., T. Kitamura, M. Anzai, W. Endo, T. Inui, Y. Takezawa, S. Suzuki-Muromoto, T. Miyabayashi, N. Togashi, H. Oba, et al. 2017. A patient with Muenke syndrome manifesting migrating neonatal seizures. *Brain Dev.* 39:873–876. https://doi.org/10.1016/j.braindev.2017.05.007

Pannier, S., V. Couloigner, N. Messaddeq, M. Elmaleh-Bergès, A. Munnich, R. Romand, and L. Legeai-Mallet. 2009. Activating Fgfr3 Y367C mutation

causes hearing loss and inner ear defect in a mouse model of chondrodysplasia. *Biochim. Biophys. Acta (BBA) - Mol. Basis Dis.* 1792:140–147. https://doi.org/10.1016/j.bbadis.2008.11.010

Peters, K., D. Ornitz, S. Werner, and L. Williams. 1993. Unique expression pattern of the FGF receptor 3 gene during mouse organogenesis. *Dev. Biol.* 155:423–430. https://doi.org/10.1006/dbio.1993.1040

de Planque, C.A., S.A. Wall, L. Dalton, G. Paternoster, É. Arnaud, M.-L.C. van Veelen, S.L. Versnel, D. Johnson, J. Jayamohan, and I.M.J. Mathijssen. 2021. Clinical signs, interventions, and treatment course of three different treatment protocols in patients with Crouzon syndrome with acanthosis nigricans. *J.Neurosurg. Pediatr.* 28:425–431. https://doi.org/10.3171/2021.2.PEDS20933

Pringle, N.P., W.-P. Yu, M. Howell, J.S. Colvin, D.M. Ornitz, and W.D. Richardson. 2003. Fgfr3 expression by astrocytes and their precursors: Evidence that astrocytes and oligodendrocytes originate in distinct neuroepithelial domains. *Development*. 130:93–102. https://doi.org/10.1242/dev.00184

Priore, R., L. Dailey, and C. Basilico. 2006. Downregulation of Akt activity contributes to the growth arrest induced by FGF in chondrocytes. *J.Cell Physiol.* 207:800–808. https://doi.org/10.1002/jcp.20620

Raybaud, C., and C. Di Rocco. 2007. Brain malformation in syndromic craniosynostoses, a primary disorder of white matter: A review. *Childs Nerv. Syst.* 23:1379–1388. https://doi.org/10.1007/s00381-007-0474-7

Richtsmeier, J.T., and K. Flaherty. 2013. Hand in glove: Brain and skull in development and dysmorphogenesis. *Acta Neuropathol.* 125:469–489. https://doi.org/10.1007/s00401-013-1104-y

Robin, N.H., M.J. Falk, and C.R. Haldeman-Englert. 1993. FGFR-related craniosynostosis syndromes. In GeneReviews. M.P. Adam, H.H. Ardinger, R.A. Pagon, S.E. Wallace, L.J. Bean, K. Stephens, A. Amemiya, editors. University of Washington, Seattle, WA

Sakamoto, K., K. Karelina, and K. Obrietan. 2011. CREB: A multifaceted regulator of neuronal plasticity and protection. *J. Neurochem.* 116:1–9. https://doi.org/10.1111/j.1471-4159.2010.07080.x

Shioda, N., and K. Fukunaga. 2017. Physiological and pathological roles of CaMKII-PP1 signaling in the brain. *Int. J. Mol. Sci.* 19:20. https://doi.org/10.3390/ijms19010020

Stevens, H.E., G.Y. Jiang, M.L. Schwartz, and F.M. Vaccarino. 2012. Learning and memory depend on fibroblast growth factor receptor 2 functioning in hippocampus. *Biol. Psychiatr.* 71:1090–1098. https://doi.org/10.1016/j.biopsych.2012.03.013

Su, N., X. Xu, C. Li, Q. He, L. Zhao, C. Li, S. Chen, F. Luo, L. Yi, X. Du, et al. 2010. Generation of Fgfr3 conditional knockout mice. *Int. J. Biol. Sci.* 6:327–332. https://doi.org/10.7150/ijbs.6.327

Thomson, R.E., P.C. Kind, N.A. Graham, M.L. Etherson, J. Kennedy, A.C. Fernandes, C.S. Marques, R.F. Hevner, and T. Iwata. 2009. Fgf receptor 3 activation promotes selective growth and expansion of occipitotemporal cortex. *Neural Dev.* 4:4. https://doi.org/10.1186/1749-8104-4-4

Thomson, R.E., F. Pellicano, and T. Iwata. 2007. Fibroblast growth factor receptor 3 kinase domain mutation increases cortical progenitor proliferation via mitogen-activated protein kinase activation. *J. Neurochem.* 100:1565–1578. https://doi.org/10.1111/j.1471-4159.2006.04285.x

Timberlake, A.T., J. Choi, S. Zaidi, Q. Lu, C. Nelson-Williams, E.D. Brooks, K. Bilguvar, I. Tikhonova, S. Mane, J.F. Yang, et al. 2016. Two locus inheritance of non-syndromic midline craniosynostosis via rare SMAD6 and common BMP2 alleles. *eLife*. 5:e20125. https://doi.org/10.7554/eLife.20125

Timberlake, A.T., S.C. Jin, C. Nelson-Williams, R. Wu, C.G. Furey, B. Islam, S. Haider, E. Loring, A. Galm, Yale Center for Genome Analysis, et al. 2019. Mutations in TFAP2B and previously unimplicated genes of the BMP, Wnt, and Hedgehog pathways in syndromic craniosynostosis. *PNAS*. 116:15116–15121. https://doi.org/10.1073/pnas.1902041116

Twigg, SR, C. Healy, C. Babbs, J.A. Sharpe, W.G. Wood, P.T. Sharpe, G.M. Morriss-Kay, A.O. Wilkie. 2009. Skeletal analysis of the Fgfr3P244R mouse, a genetic model for the Muenke craniosynostosis syndrome. *Dev Dyn.* 238:331–342. https://doi.org/10.1002/dvdy.21790.

Twigg, S.R.F., and A.O.M. Wilkie. 2015. A genetic-pathophysiological framework for craniosynostosis. *Am. J. Hum. Genet.* 97:359–377. https://doi.org/10.1016/j.ajhg.2015.07.006

Vithayathil, J., J. Pucilowska, L.H. Goodnough, R.P. Atit, and G.E. Landreth. 2015. Dentate gyrus development requires ERK activity to maintain progenitor population and MAPK pathway feedback regulation. *J. Neurosci.* 35:6836–6848. https://doi.org/10.1523/JNEUROSCI.4196-14.2015

Wilkie, A.O.M., J.C. Byren, J.A. Hurst, J. Jayamohan, D. Johnson, S.J.L. Knight, T. Lester, P.G. Richards, S.R.F. Twigg, and S.A. Wall. 2010. Prevalence and complications of single gene and chromosomal disorders in craniosynostosis. *Pediatrics*. 126:e391–e400. https://doi.org/10.1542/peds.2009-3491

Yarnell, C.M.P., Y.A. Addissie, D.W. Hadley, M.J. Guillen Sacoto, N.B. Agochukwu, R.A. Hart, E.A. Wiggs, P. Platte, Y. Paelecke, H. Collmann, et al. 2015. Executive function and adaptive behavior in Muenke syndrome. *J. Pediatr.* 167:428–434. https://doi.org/10.1016/j.jpeds.2015.04.080

Yu, M., L. Ma, Y. Yuan, X. Ye, A. Montagne, J. He, T.-V. Ho, Y. Wu, Z. Zhao, N. Sta Maria, et al. 2021. Cranial suture regeneration mitigates skull and neurocognitive defects in craniosynostosis. *Cell*. 184:243–256.e18. https://doi.org/10.1016/j.cell.2020.11.037

Zhao, M., D. Li, K. Shimazu, Y.-X. Zhou, B. Lu, and C.-X. Deng. 2007. Fibroblast growth factor receptor-1 is required for long-term potentiation, memory consolidation, and neurogenesis. *Biol. Psychiatry*. 62:381–390. https://doi.org/10.1016/j.biopsych.2006.10.019

JEM

Supplemental material

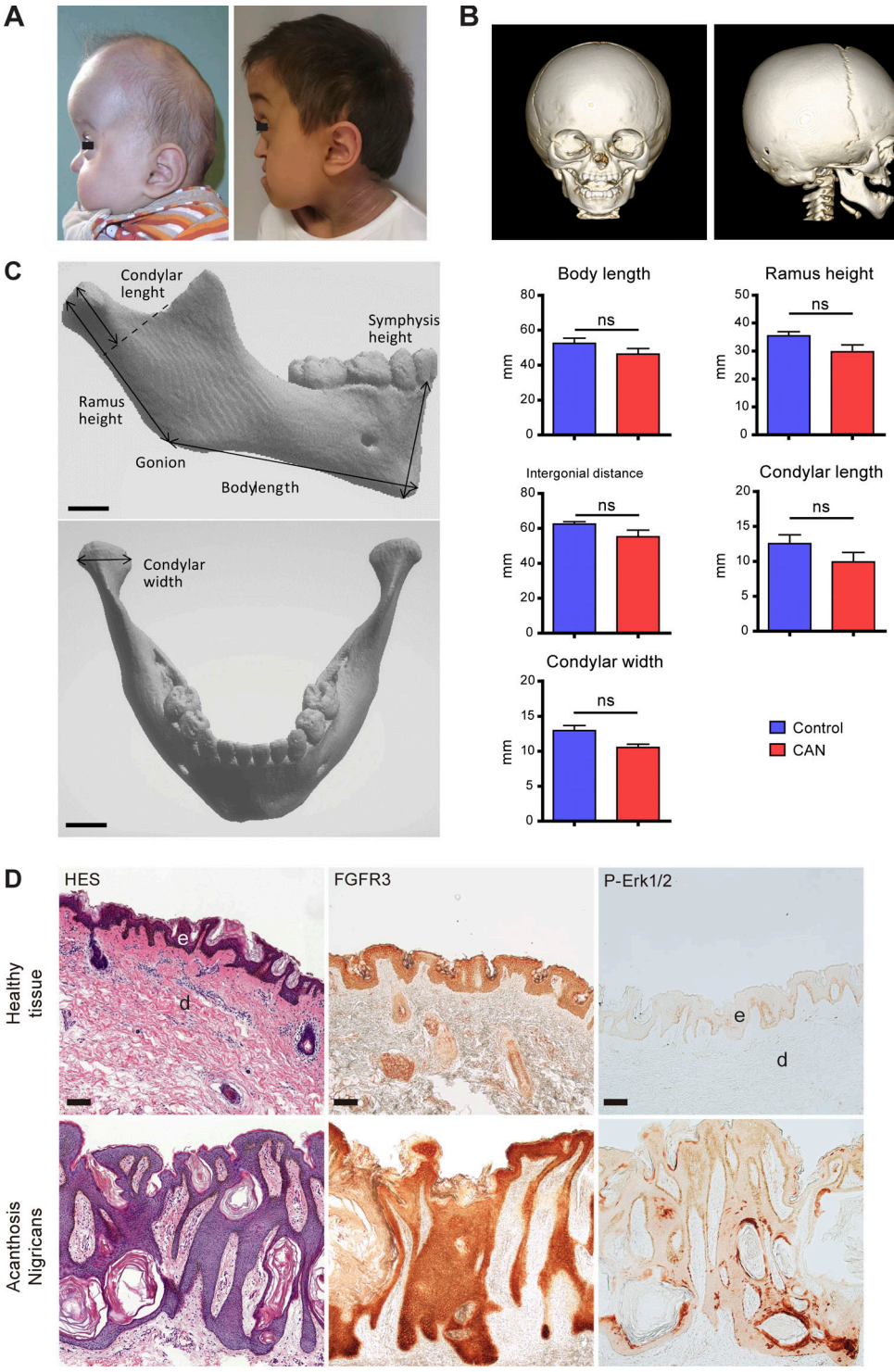

Figure S1. **Clinical features of CAN. (A)** Craniofacial features of CAN patient #1 at the age of 11 mo and 2 yr, with brachycephaly, midface hypoplasia, bulging eyes, and an underdeveloped upper jaw. The late appearance of acanthosis nigricans is visible, especially on skin folds of the neck (right panel). **(B)** CT scan of patient #2 at 1 yr of age, showing facial retrusion and posterior vault thumbprinting. **(C)** Mandible measurements. Symphysis height was measured from the highest aspect of the alveolar bone to the lowest point of the basilar contour of the symphysis. Condylar length was estimated as the distance between the highest aspects of the condyle above and below the intersection of a perpendicular line with the condyle–gonion line (the dotted line) passing through the sigmoid notch. Condylar width was measured at the widest point in the coronal plane. Measurements were performed on the right aspect of the mandible. The intergonial distance was measured between the left and right gonion. Measurements in four patients with CAN (median [IQR] age: 22.7 mo [12.6; range: 8–31.3]), relative to four age- and sex-matched controls. **(D)** Stained paraffin sections of healthy skin (left) and acanthosis nigricans areas (right) from patient #1 at the age of 11 yr. Hematoxylin–eosin staining (HES, top panel) revealed hyperkeratosis, hair follicle hyperplasia, and cyst formation. The middle and lower panels show slides stained for FGFR3 and Erk1/2. Data are expressed as the mean ± SEM; ns, not significant in a two-tailed Student's *t* test, relative to the control group. Scale bar: 100 µm. e, epidermis; d, dermis.

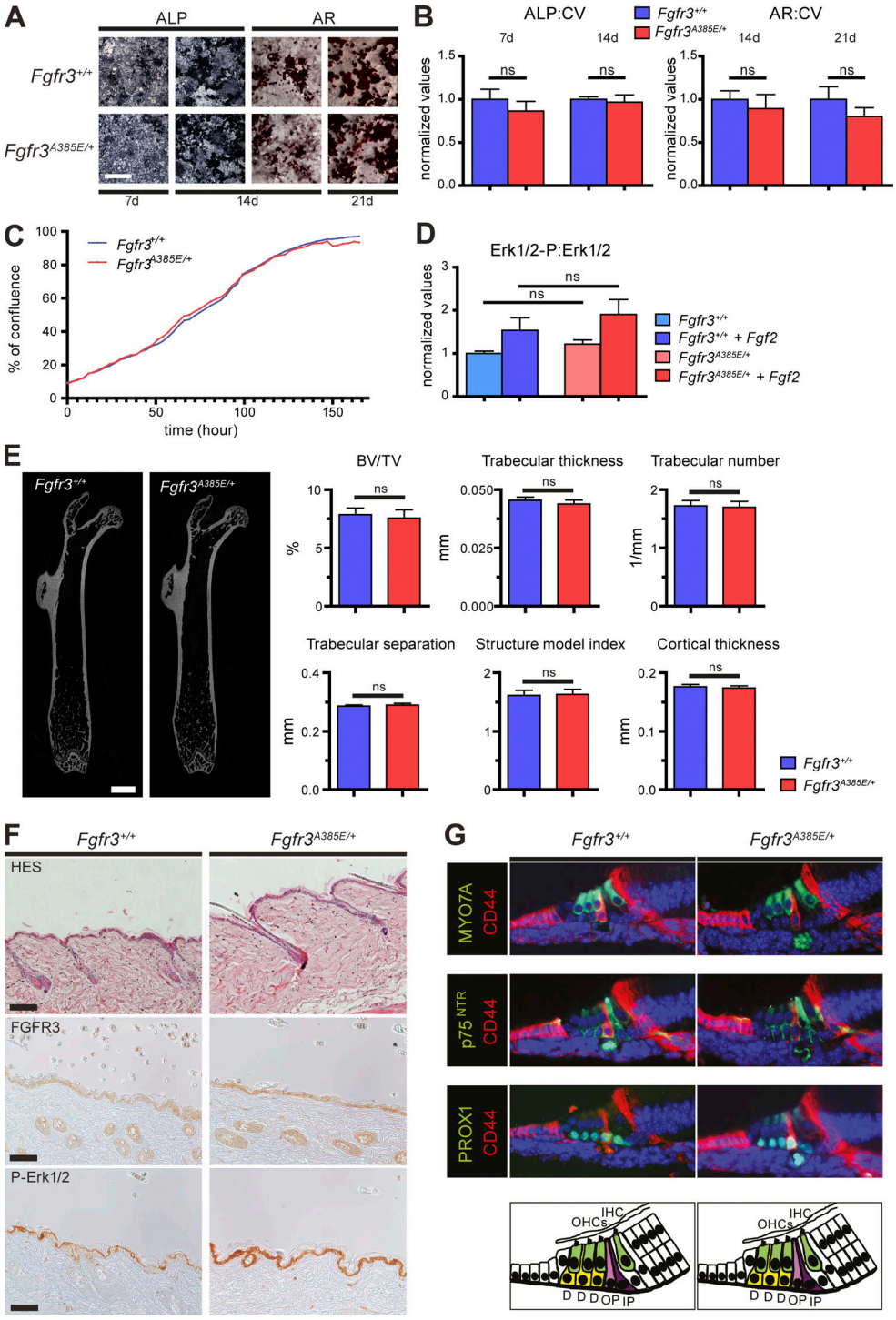

Figure S2. **Normal bone, skin, and inner ear phenotype in *Fgfr3*$^{A385E/+}$ mice. (A)** Calvarial osteoblast culture. ALP activity and Alizarin Red (AR) staining of osteoblasts isolated from calvaria of *Fgfr3*$^{+/+}$ and *Fgfr3*$^{A385E/+}$ mice (7 d: *Fgfr3*$^{+/+}$, n = 6; *Fgfr3*$^{A385E/+}$, n = 5; 14–21 d: *Fgfr3*$^{+/+}$, n = 9; *Fgfr3*$^{A385E/+}$, n = 8). NS in an unpaired Student's t test. Scale bar: 3 mm. **(B)** Quantification of ALP activity and AR staining, normalized against crystal violet staining (CV). **(C)** Osteoblast proliferation was assessed using the Incucyte cell imaging system. **(D)** Quantification of the P-Erk1/2:Erk1/2 ratio in n = 5 independent immunoblot experiments. Data are expressed as the mean ± SEM. *, P ≤ 0.05; **, P ≤ 0.01; ***, P ≤ 0.001; ns,: not significant in an ANOVA with Tukey's post-hoc test for multiple comparisons. **(E)** A representative µCT scan of the femur in 3-mo-old male *Fgfr3*$^{A385E/+}$mice (n = 9) and *Fgfr3*$^{+/+}$ mice (n = 9). Bar graphs show the bone volume fraction (bone volume/trabecular volume), trabecular thickness, trabecular number, trabecular separation, the structure model index, and cortical thickness. **(F)** Histological analysis of mouse skin. Longitudinal back skin sections from 10-week-old *Fgfr3*$^{A385E/+}$ and *Fgfr3*$^{+/+}$ mice (n = 4 in each group) were stained with hematoxylin–eosin (top panel) or analyzed immunohistochemically for *Fgfr3* (middle panel) or p-Erk1/2 (lower panel). Scale bar: 50 µm. **(G)** Inner ear analysis. Organ of Corti from *Fgfr3*$^{A385E/+}$ mice (n = 4) and *Fgfr3*$^{+/+}$ mice (n = 4) on P3. Immunofluorescence for CD44 (outer pillar cells), MYO7A (hair cells), p75^{NTR} (inner pillar cells), and PROX1 (support-cell nuclei). D, Deiters' cells; IHCs, inner hair cells; IPCs, inner pillar cells; OHCs, outer hair cells; OPCs, outer pillar cells. Data are expressed as the mean ± SEM. ns, not significant in a two-tailed Student's t test, relative to the control group.

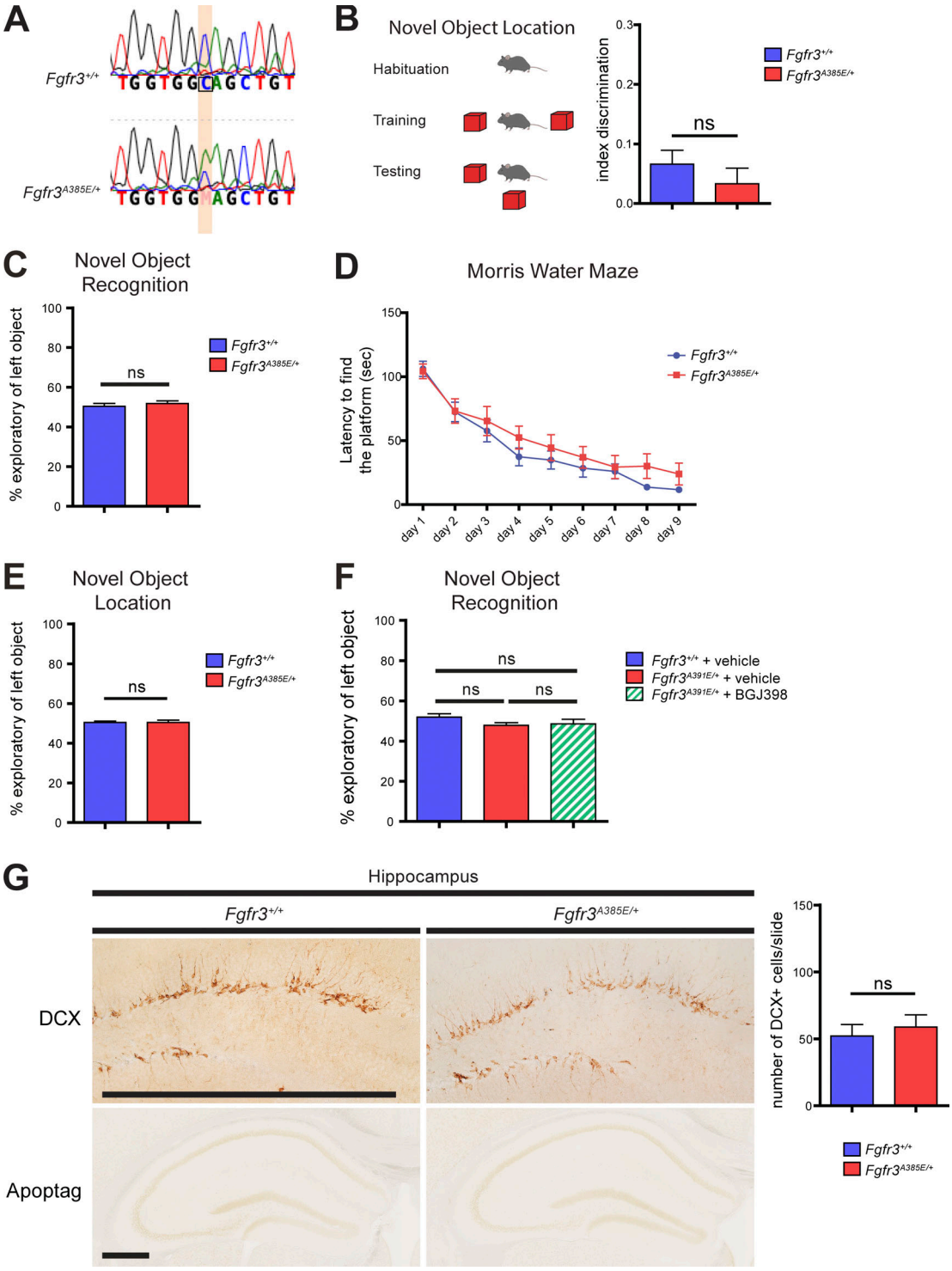

Figure S3. **Hippocampal neurogenesis and cell survival. (A)** Detection of the heterozygous mutation p.Ala385Glu in RNA isolated from the hippocampus of 4-mo-old mice. **(B)** The NOL test performed in two independent groups of 4-mo-old male animals. The discrimination index was measured 24 h after the training phase, in order to assess the memory performance of *Fgfr3*$^{A385E/+}$ mice and their control littermates (*Fgfr3*$^{+/+}$, *n* = 21; *Fgfr3*$^{A385E/+}$, *n* = 20). **(C)** The recording from the NOR test. Percentage time exploring both objects during the NOR test training phase (Fig 3 B). The animals explored the two similar objects to the same extent (*Fgfr3*$^{+/+}$, *n* = 17; *Fgfr3*$^{A385E/+}$, *n* = 14). **(D)** The MWM test performed on 4-mo-old animals (*Fgfr3*$^{+/+}$, *n* = 17; *Fgfr3*$^{A385E/+}$, *n* = 14) over 9 d. **(E)** Percentage time exploring both objects during the NOL test training phase (Fig 3 D). The animals explored the two similar objects to the same extent (*Fgfr3*$^{+/+}$, *n* = 12; *Fgfr3*$^{A385E/+}$, *n* = 9). **(F)** Percentage time exploring both objects during the NOR test training phase, after 7 d of BGJ398 injection (Fig 4 F). The animals explored the two similar objects to the same extent (*Fgfr3*$^{+/+}$ + vehicle, *n* = 15; *Fgfr3*$^{A385E/+}$ + vehicle, *n* = 14; *Fgfr3*$^{A385E/+}$ + BGJ398, *n* = 14). An ANOVA with Tukey's post-hoc test for multiple comparisons and an unpaired Student's *t* test. **(G)** Representative Apoptag (TUNEL) staining performed on six consecutive hippocampus slides per individual (*Fgfr3*$^{+/+}$, *n* = 6; *Fgfr3*$^{A385E/+}$, *n* = 6). Immunohistochemistry for doublecortin (DCX), with the number of DCX-labeled cells in *Fgfr3*$^{+/+}$ (*n* = 8) and *Fgfr3*$^{A385E/+}$ (*n* = 12) animals. Scale bar: 500 µm.